Compositional analysis of Sindbis virus ribonucleoproteins reveals an extensive co-opting of key nuclear RNA-binding proteins

Wael Kamel[1,2], Vincenzo Ruscica[2], Manuel Garcia-Moreno[2], Natasha Palmalux[1], Louisa Iselin[1,2,3], Maximilian Hannan[2], Aino Järvelin[2], Marko Noerenberg[1], Samantha Moore[2], Andres Merits[4], Ilan Davis[2], Javier Martinez[5], Shabaz Mohammed*[2,6,7] and Alfredo Castello*[1,2]

1. MRC-University of Glasgow Centre for Virus Research, G61 1QH, Glasgow, Scotland (UK).

2. Department of Biochemistry, University of Oxford, South Parks Road, OX1 3QU, Oxford, UK.

3. Nuffield Department of Medicine, Peter Medawar Building for Pathogen Research, University of Oxford, Oxford, OX1 3SY, UK

4. Institute of Technology, University of Tartu, Tartu, 50411, Estonia

5. Center of Medical Biochemistry, Max Perutz Labs, Medical University of Vienna, Vienna, Austria.

6. Department of Chemistry, University of Oxford, Mansfield Road, Oxford, OX1 3TA, UK

7. The Rosalind Franklin Institute, Oxfordshire, OX11 0FA, UK

*, Corresponding author

Abstract

The expansion of tropical mosquito habitats and associated arboviruses is a risk for human health, and it thus becomes fundamental to identify new antiviral strategies. In this study we employ a new approach to elucidate the composition of the ribonucleoproteins (RNPs) of a prototypical arbovirus called Sindbis (SINV). SINV RNPs contain 453 cellular and 6 viral proteins, many of these proteins are nuclear in uninfected cells and redistribute to the cytoplasm upon infection. These findings suggest that SINV RNAs act as ’spiderwebs’, capturing host factors required for viral

replication and gene expression in the cytoplasm. Functional perturbation of several of these host proteins causes profound effects in virus infection, as illustrated here with the tRNA ligase complex. Moreover, inhibition of viral RNP components with available drugs hampers the infection of a wide range of viruses, opening new avenues for the development of broad-spectrum therapies.

Research highlights

- SINV RNA interactome includes 453 cellular and 6 viral proteins.
- Nuclear RBPs that interact with SINV RNA are selectively redistributed to the cytoplasm upon infection
- The tRNA ligase complex plays major regulatory roles in SINV and SARS-CoV-2 replication
- The SINV RNA interactome is enriched in pan-viral regulators with therapeutic potential.

INTRODUCTION

The alphavirus genus contains several arthropod-borne viruses (arboviruses) that can cause disease in humans (Kurkela et al., 2004; Laine et al., 2004; Marks and Marks, 2016; Silva and Dermody, 2017), including Chikungunya (CHIKV), Venezuelan equine encephalitis virus (VEEV), Ross river virus (RRV), Semliki forest virus (SFV) and Sindbis virus (SINV). These arboviruses grow in the salivary glands of mosquitoes from the *Aedes* family and are transmitted to the human host through their bites (Lim et al., 2018). The habitats of the main vectors for alphaviruses, *Aedes aegypti and Aedes albopictus*, are expanding due to global warming and international trade, raising concerns about the emergence of arboviral outbreaks and epidemics (Bonizzoni et al., 2013). Therefore, it has become crucial to improve our understanding of the host-virus interactions underpinning alphavirus infection in order to identify potential targets for therapeutic intervention.

Alphaviruses have single stranded (ss), positive sense RNA genomes ~11kb that are capped and polyadenylated, resembling cellular mRNAs. Because of the limited coding capacity of their genomes, alphaviruses heavily rely on cellular proteins to complete the viral life cycle (Strauss and Strauss, 1994). The genomic (g)RNA of alphavirus plays a dual role in infection, acting as genome but also as messenger

(m)RNA. It is thus a hub for crucial host-virus interactions that regulate the viral life cycle (Garcia-Moreno et al., 2018; Iselin et al., 2021). Cellular RNA-binding proteins (RBPs) are indeed involved in virtually every step of alphavirus life cycle, and can play pro- or antiviral roles (Balistreri et al., 2014; Carrasco et al., 2018; Dicker et al., 2020; Garcia-Moreno et al., 2019; Kim et al., 2020). However, the complement of RBPs that engage with viral RNA (vRNA) in infected cells have remained largely unknown.

Over the last few years, several approaches have been developed to elucidate the composition of viral ribonucleoproteins (vRNPs) within cells, and two of these have been applied to alphaviruses (Iselin et al., 2021). Viral cross-linking and solid-phase purification (VIR-CLASP) was recently used to study the scope of protein-RNA interactions mediated by alphavirus RNA after entry into the cell (Kim et al., 2020). It employs viral particles containing vRNA labelled with the photo-activatable nucleotide 4-thiouridine (4SU). Using this labelled vRNA as a bait, VIR-CLASP revealed that the gRNA of alphaviruses establishes functionally important interactions with hundreds of cellular RBPs during the initial steps of infection (Kim et al., 2020). To profile how these protein-RNA interactions evolve in conditions where viral replication is already active, an alternative method named cross-link-assisted mRNP purification (CLASP) was developed (Gebhart et al., 2020; LaPointe et al., 2018). CLASP employs 4SU labelling of vRNA, followed by formaldehyde crosslinking, 4SU biotinylation and streptavidin purification coupled with proteomics (Gebhart et al., 2020; LaPointe et al., 2018). Although informative, CLASP datasets had a very low incidence of *bona fide* RBPs likely due to the promiscuous nature of formaldehyde crosslinking and/or limited specificity in the purification of vRNA, calling for alternative approaches (Iselin et al., 2021).

To fill this gap in our understanding of post-replicative alphavirus RNPs, we have developed a novel proteome-wide approach called viral RNA interactome capture (vRIC) (Kamel et al., 2021). Here we show that the RNAs of the prototypical alphavirus Sindbis virus (SINV) interact with 453 cellular and 6 viral proteins. SINV RNPs contain host proteins involved in a broad range of processes, including translation, RNA decay, splicing, formation of RNA granules and immunity. Amongst these, we noticed a pool of nuclear proteins that redistribute to the cytoplasm upon infection, probably trapped by vRNA. Functional assays reveal that SINV RNP components play critical

roles not only in SINV infection, but in a broad range of viruses. For example, the tRNA ligase complex (tRNA-LC) regulates both SINV and SARS-CoV-2 infection (Kamel et al., 2021). Moreover, experiments with available inhibitors revealed that cellular RBPs are promising targets for broad-spectrum antiviral therapies.

RESULTS AND DISCUSSION

Elucidating the composition of SINV RNPs

SINV infection causes a profound remodelling of the cellular RNA-binding proteome (RBPome) (Garcia-Moreno et al., 2019). This implies that the pool of cellular RBPs that can engage vRNA varies throughout the infection. To discover the subset of cellular RBPs that bind to SINV RNA after the initial burst of viral RNA replication, we applied a new method named vRIC to SINV-infected cells. Upon infection with SINV, cells are treated with 4SU together with a choice of inhibitor of cellular RNA polymerases (RNAPs) (Figure 1A). Since viral RNA-dependent RNA polymerases (RdRps) are typically refractory to such inhibitors, 4SU is primarily redirected into newly synthesised vRNA. vRNA is then crosslinked to RBPs in intimate contact ('zero distance') by activation of 4SU molecules with UV light at 365 nm. Upon lysis under denaturing conditions, proteins covalently bound to vRNA are isolated with oligo(dT) magnetic beads under stringent washes, eluted by heat and RNase treatment, and analysed by quantitative mass spectrometry (Figure 1A). vRIC performance relies in two key steps that require optimisation: i) the inhibition of the cellular RNAPs and ii) the incorporation of 4SU into nascent vRNA.

Initially, we tested the effects of the RNAP inhibitors actinomycin D (ActD), 5,6-dichloro-1-beta-D-ribofuranosylbenzimidazole (DRB) and flavopiridol (Fvo) (Bensaude, 2011) in cellular mRNA transcription and viral RNA replication (Figure S1A). Using a chimeric virus that expresses mCherry from a duplicated subgenomic promoter (SINV-mCherry) (Garcia-Moreno et al., 2019), we observed that neither DRB nor Fvo have detrimental effects on viral fitness (Figure S1A). Conversely, ActD caused a substantial reduction in viral gene expression, suggesting potential side effects in viral replication. To test the ability of these compounds to inhibit RNAPII, we employed a cell line with inducible expression of eGFP from a strong cytomegalovirus promoter controlled by deoxycycline (Dox). ActD and, particularly, Fvo strongly

suppressed eGFP expression, whereas DRB had only a mild effect (Figure S1B). Therefore, we selected Fvo for further experiments since it strongly inhibits RNAPII transcription while causing negligible effects on SINV gene expression.

Next, we optimised the 4SU pulse, aiming for efficient incorporation into vRNA without affecting viral replication. When SINV-mCherry and 4SU were added simultaneously to cells, viral gene expression was inhibited in a dose-dependent manner (Figure S1C and D). The inhibitory effect of 4SU was prevented when its addition was delayed for 2h (Figure S1E). 4SU and Fvo were also non-toxic for SFV (Figure S1F) and SARS-CoV-2 (Kamel et al., 2021) when added after 2 hours post infection (hpi), which indicates that vRIC can be adapted to a wide range of viruses.

To elucidate the composition of SINV RNPs, we implemented the optimised conditions into the vRIC protocol and applied it to SINV-infected cells. We included in our proteomic analyses (Figure S2A-E) all the controls schematised in Figure 1B to monitor several experimental variables including the efficiency and specificity of 4SU incorporation into vRNA and the performance of UV_{365} crosslinking. In the absence of 4SU (M/-/-) and virus, the overall protein intensity observed in oligo(dT) eluates was low (Figure S2F), leading to a remarkably 'clean' lane when subjected to silver staining analysis (Figure 1C, third lane). Conversely, addition of 4SU and UV_{360} (M/4SU/-) led to the isolation of a complex protein set that resembles the previously established cellular RBPomes (Figure 1C, first lane and S2F) (Beckmann et al., 2015; Castello et al., 2012). Importantly, addition of Fvo (M/4SU/Fvo) strongly reduced protein isolation, reflecting a lack of 4SU incorporation into cellular poly(A) RNAs (Figure 1C second lane and S2F). Indeed, principal component analysis (PCA) revealed that M/4SU/- and M/4SU/Fvo separated in PC1 even though they only differ in the presence of Fvo (Figure 1E).

For comparative purposes with SINV RNPs, we next defined the composition of cellular (c)RNPs by analysing the mock samples treated with and without 4SU (M/4SU/- and M/-/-). The proteomic analysis revealed 797 proteins significantly enriched in oligo(dT) eluates in a 4SU-dependent manner, 723 with 1% false discovery rate (FDR) plus an additional 74 with 10% FDR (Figure 1F, Table 1). As expected, these proteins are heavily enriched in known RBPs, with 83% of the proteins previously identified by RNA interactome capture (RIC) studies in human cells (Hentze

et al., 2018). We noticed that a small set of 144 RBPs were enriched in Fvo-treated mock samples (M/4SU/Fvo) over Fvo-untreated ones (M/4SU/-), with 'mitochondrial mRNA processing' factors being dominant amongst them (Figure 1G-I, Table 3). These proteins likely derive from the isolation of mitochondrial RNAs as they have poly(A) tail in mammalian cells (Temperley et al., 2010), and RNAPII inhibitors do not affect the mitochondrial RNAP (Barchiesi and Vascotto, 2019; Dhir et al., 2018). We refer to this group of Fvo-insensitive proteins as mitoRNP given the prevalence of mitochondrial proteins.

In contrast to uninfected cells, a rich protein pattern was observed in SINV-infected cells, even in presence of Fvo (Figure 1C, lanes 4 and 5). These results agree with notion that viral RdRps are insensitive to Fvo enabling 4SU incorporation. SINV capsid, known to interact with SINV RNA (Garcia-Moreno et al., 2019; Sokoloski et al., 2017), was highly enriched in oligo(dT) eluates from infected cells (Figure 1D). Fvo treatment reduced the isolation of RBPs in SINV infected cells when compared to untreated samples (Figure S2G-H), reflecting that the contribution of cellular RNAs is reduced in a Fvo-dependent manner.

vRIC revealed 459 RBPs (345 with 1% FDR plus an additional 114 with 10% FDR, Table 4) that are enriched in SINV-infected samples (V/4SU/Fvo) over the mock control (M/4SU/Fvo) (Figure 2A). These RBPs are referred henceforth to as viral (v)RNP components. Gene ontology (GO) analysis revealed that SINV RNPs are enriched in terms related to the viral life cycle, including viral RNA translation initiation and termination, stress granules and cytokine production (Figure 2B). We reasoned that if the proteins uncovered by vRIC are *bona fide* components of SINV RNPs, then they must localise in the cytoplasmic foci where SINV replication occurs, known as viral factories (i.e. CPV-1, cytopathic vacuole type 1). To test this hypothesis we used immunofluorescence localisation data from eGFP-tagged RBPs expressed in SINV-infected cells (Garcia-Moreno et al., 2019). Interestingly, 8 out of 10 (80%) of the proteins identified SINV RNP components are enriched in viral factories in microscopy experiments (Figure 2C). Altogether, these results support the idea that vRIC-identified RBP do interact with SINV RNA.

vRNPs are composed of a heterogenous populations of RBPs with different functional domains, reflecting the complex processes taken place in the vRNA

microenvironment. The vRNP components include kinases (21), among which are the key innate immunity player EIF2AK2 (PKR) (Hull and Bevilacqua, 2016), the mitogen-activated protein kinase MAP4K4 that regulates inflammatory responses (Aouadi et al., 2009), and SRPK1 which was previously shown to promote SINV and human immunodeficiency virus type 1 (HIV-1) infection (Fukuhara et al., 2006; Garcia-Moreno et al., 2019). In addition, we noticed the presence of proteins involved in ubiquitination pathway, including 9 E3 ligases (MKRN2, RC3H1, TRIM56, TRIM26, LTN1, NFX, NXFL1, RBBP6 and UHRF1); and 6 deubiquitinating enzymes (OTUD4, USP10, USP16, USP36, USP42 and ALG13). Interestingly, we recently showed that TRIM56 RNA-binding activity is triggered after SINV and SARS-CoV-2 infection, correlating with its accumulation in the viral replication factories and a suppressive effect in infection (Garcia-Moreno et al., 2019; Kamel et al., 2021). TRIM56, together with the enzymes listed above, may well be new cases of 'riboregulation' (Hentze et al., 2018; Iselin et al., 2021), a process by which protein function can be allosterically regulated by RNA biding, as it is the case for EIF2AK/PKR (Hull and Bevilacqua, 2016), TRIM25 (Choudhury et al., 2017; Haubrich et al., 2020) and SQSTM1/p62 (Horos et al., 2019). Other prominent group across vRNP components are RNA helicases with 28 representatives, including DDX1 (see below), DHX36 and DDX21 that with TRIF act as dsRNA sensor in the antiviral response (Zhang et al., 2011b), and DDX3X which is known for its pivotal roles in virus infection (Hernandez-Diaz et al., 2021). In addition, 12 nucleases can be detected in vRNPs covering endonucleases (e.g. AGO2, SND1, SMG6 and others), 5' to 3' exonucleases (XRN1), and 3' to 5' exonucleases (EXOSC10).

Although SINV subgenomic RNA is capped and polyadenylated, its translation does not require the cap-binding protein EIF4E and the factor involved in the delivery of the methionine tRNA at initiation codons EIF2S1 (EIF2α) (Carrasco et al., 2018; Castello et al., 2006; Ventoso et al., 2006). However, whether these two key initiation factors engage or not with SINV RNPs remains unknown. EIF4E and EIFS1/EIF2α are typically found by RNA interactome capture interacting with cellular mRNAs (Hentze et al., 2018; Kamel et al., 2021); however, they are not detected in SINV RNPs despite the presence of the other members of the EIF4F complex (EIF4G1-3, EIF4B and EIF4A1) and several of the subunits of EIF3 (A, C, D and G). EIF4E is also not detected in SARS-CoV-2 RNPs (Flynn et al., 2021; Kamel et al., 2021; Lee et al.,

2021; Schmidt et al., 2020), which suggests that capped viral RNAs may initiate translation in an EIF4E-independent manner in infected cells.

Similarities and divergences between cellular and viral RNPs

Next, we tested if cRNPs (M/4SU/- vs M/-/-), mitoRNPs (M/4SU/Fvo vs M/4SU/-) and vRNPs (M/4SU/Fvo vs M/4SU/-) are compositionally distinct. Interestingly, cRNPs and vRNPs shared over 50% of their components, while nearly no overlap was observed with mitoRNPs (Figure 2D). These results suggest that cRNPs and vRNPs are relatively similar, and both strongly differ from mitoRNPs. This result also hints that mitoRNPs are negligible both in terms of the number of proteins and their abundance, making them only observable in the negative control where the cRNPs and vRNPs are absent. Moreover, nearly 50% of the proteins in the vRNP and cRNP sets harbour well-established RNA-binding domains (RBDs), with equal distribution of both classical and non-canonical RBDs (Figure 2E) [definition of these domain types in (Castello et al., 2012)]. However, mitoRNP components and proteins enriched only in vRNPs (vRNPen) have a higher incidence of non-canonical and unknown RBDs (Figure 2E and S2I), invoking functions beyond classic roles in RNA biology. Intrinsic protein disorder is a common feature found across RBPs that plays prevalent roles in RNA binding (Castello et al., 2012; Castello et al., 2016; Jarvelin et al., 2016). In agreement, the incidence of intrinsically disorder regions (IDRs) within vRNP and cRNP components is similar, opposite to mitoRNPs, which are known to be depleted in IDRs (Figure 2F and S2J) (Fukuchi et al., 2011). Altogether these results suggest that vRNP and cRNP, while partially distinct in composition, share major properties that are not common in mitoRNPs.

To further understand the differences between vRNP and cRNP components, we analysed their binding profiles, when available, using the ENCODE-eCLIP database (Van Nostrand et al., 2016). vRNPs and cRNPs include 140 proteins with eCLIP data and we grouped them based on their binding preferences within the RNA architecture (Figure 2H). Interestingly, vRNP components are enriched in RBPs that typically bind to 5’ and 3’ untranslated regions (UTRs), while cRNPs have a higher proportion of intron binding RBPs. This compositional bias highlights the importance of the 5’ and

3' UTRs of SINV RNAs for replication and translation and the lack of RNA splicing in the alphavirus life cycle (Carrasco et al., 2018; Strauss and Strauss, 1994).

Unveiling the subset of SINV proteins that interact with vRNA

vRIC identified six viral proteins within vRNPs, which includes the non-structural proteins nsP1, nsP2, nsP3 and nsP4 and the structural proteins caspid and E2 (Figure 2A, S2K and Table 4). To determine whether these viral proteins are captured due to a *bona fide* interaction with RNA or because of their high abundance in infected cells, we normalized their intensities in vRIC eluates to those in the whole cell proteome (Figure 2H). Capsid displayed the highest "crosslink-ability", as expected from its involvement in the packing of viral genomes into virions (Sokoloski et al., 2017). It was followed by the non-structural proteins, which are essential for viral replication (Figure 2I), including the capping enzyme nsP1, the helicase nsP2 and the RNA-dependent RNA polymerase nsP4. Interestingly, we noticed that nsP3 also interacts with vRNA in infected cells, but unlike the other non-structural proteins, nsP3 potential interaction with vRNA remains poorly understood (Gotte et al., 2018). Recently, it was proposed that CHIKV nsP3 interacts with vRNA through its AUD domain (Gao et al., 2019). To test this possibility, we analysed nsP3 with a software that predicts RBDs based on sequence similarities with the RNA-binding sites present in human RBPs (Castello et al., 2016; Kamel et al., 2021). Consistently, our results revealed a high-confidence RNA-binding site placed at the AUD domain (Figure 2I). While the nsP3 peptide coverage was high in vRIC eluates, supporting that it binds to vRNA (Figure 2I), its crosslinking efficiency was substantially lower than that of the other nsPs (Figure 2H), likely reflecting a more transitory or geometrically suboptimal interaction with vRNA. Surprisingly, vRIC data showed that E2 also interacts with RNA (Figure 2H), in agreement with previous results (Garcia-Moreno et al., 2019). However, E2 crosslinking efficiency is the lowest of all viral proteins, which indicates that it may establish low affinity interactions with vRNA. Similar low efficiency interactions were observed for the spike of SARS-CoV-2 (Kamel et al., 2021). The most likely scenario in which viral glycoproteins can interact with vRNA is in the interior of the viral particles, where RNA accumulates underneath the lipidic envelope, as shown by cryo-electron microscopy (Yao et al., 2020; Zhang et al., 2011a). Whether the interactions of E2 are

stochastic or play a functional role in the assembly or structural properties of viral particles requires further investigation.

vRNA hijacks nuclear RBPs in the cytoplasm

SINV replication complexes are initially formed at the plasma membrane and then transferred to endosome-derived membranous compartments in the cytoplasm (CPV-1) (Frolova et al., 2010). Surprisingly, we noticed that a substantial proportion of the proteins that interact with SINV RNA are nuclear (Figure 3A). As SINV infection causes a profound shut off of the novo protein synthesis (Carrasco et al., 2018), the most likely scenario is that this cohort of nuclear RBPs is relocated to the cytoplasm where they engage with vRNA. To test this globally, we performed nuclear/cytoplasmic fractionation of mock- and SINV-infected cells followed by quantitative proteomics. After fraction and quality control check with known nuclear and cytoplasmic proteins (Figure 3B), biological quadruplets were analysed by proteomics showing excellent intensity correlation between replicates (Figure S3A). Principal component analysis revealed that nuclear and cytoplasmic fractions differ in composition. Cytoplasmic/nuclear protein ratios remained largely unaltered by SINV infection (Figure 3C, left panels). This supports that nuclear envelope integrity is maintained upon SINV infection. However, when focusing only in vRNP components, we observed a strong increase in cytoplasmic localisation in SINV infected cells (Figure 3C, right panels). This change in location also applied to nuclear RBPs previously known to shuttle to the cytoplasm during alphavirus infection, such as ELAV1, HNRNPK, HNRNPM, HNRNPA1, TIAL1 and TIA1 (Figure S3C) (Lloyd, 2015; Sanz et al., 2015). Altogether, these data revealed that nuclear RBPs that interact with SINV RNA partially relocate to the cytoplasm upon infection.

To assess in further detail the magnitude and directionality of these changes in localisation, we generated a redistribution index for each protein (i.e. cytoplasmic/nuclear protein intensity ratio in mock versus infected cells) (Figure S3D). Cellular proteins can be classified depending on their localization as i) nuclear ii) nuclear/cytoplasmic and ii) cytoplasmic, however for simplicity we grouped them into nucleus-enriched or cytoplasm-enriched (Figure S3D). Interestingly, most of the proteins within the cellular proteome with high redistribution index show strong nuclear localization ($r= -0.117$, $p <0.01$). This nuclear protein localisation bias became more

dominant when focusing exclusively in vRNP components (r= -0.35, p <0.001) (Figure 3D and S3F). Indeed, subtraction of the vRNP components from the whole proteome reduced the redistribution bias (r=-0.056, non-significant [NS]) (Figure S3E), implying that they are the main source of change. Conversely, no significant changes in the redistribution index were observed for the proteins enriched in cRNP (cRNPen; r=-0.09, NS) (Figure 3D and S3E). Altogether, this data strongly indicates that SINV RNA is the main driver for the cytoplasmic location of a defined subset of nuclear RBPs.

To validate these results, we next tested by western blotting the subcellular localisation of RBPs significantly up-or downregulated in the cytoplasmic or the nuclear fractions after SINV infection, particularly MATR3, AQR, GLTSCR2 and SFB1 (Figure 3E-G, Tables 5 and 6). Western blotting analysis revealed that all these proteins displayed an increased presence in the cytoplasm of SINV infected cells when compared to the mock control, while the location of the nuclear and cytoplasmic controls GAPDH and LaminB remained unaltered, further corroborating our results (Figure 3H). GO analysis revealed that most of the RBPs with high redistribution index are involved in splicing or have nucleolar localisation (Figure 3I). Strikingly, many of these shuttling proteins have been reported to interact with the RNA of different cytoplasmic viruses (Figure 3J) (Iselin et al., 2021), suggesting that these localisation changes may occur across many viruses. Moreover, most of the vRNP components with high redistribution index display altered RNA-binding activity after SINV infection, suggesting functional regulation (Figure 3K) (Garcia-Moreno et al., 2019).

The set of 'nuclear SINV RNP' components include several RBPs with previously established roles in virus infection. For example, the nucleolar helicase DDX56 has recently been shown to shuttle to the cytoplasm after CHIKV infection, interfering with viral replication upon interaction with vRNA (Taschuk et al., 2020). Similarly, DDX21 partially relocates to the cytoplasm after dengue virus (DENV) infection and also suppresses virus replication (Dong et al., 2016). The spliceosomal helicase AQR was recently shown to associate with polysomes in ZIKV and DENV-infected cells (Aviner et al., 2021). GLTSCR2 shuttles to the cytoplasm upon vesicular stomatitis virus (VSV) infection and hampers RIGI signalling preventing IFN-β induction (Wang et al., 2016). Altogether, our results reveal that a defined set of cellular RBPs relocalise from the

nucleus to the cytoplasm upon SINV infection, and that these changes are most likely driven by vRNA.

tRNA ligase complex is a key regulator of alphavirus infection

The tRNA ligase complex (tRNA-LC) mediates the splicing of tRNAs as well as that of the short intron present in *xbp1* mRNA (Jurkin et al., 2014; Popow et al., 2011; Popow et al., 2014). Three components of the tRNA-LC are present in SINV and SARS-CoV-2 RNPs (Kamel et al., 2021), which are the ligase subunit RTCB, DDX1 and FAM98A (Figure 2A and 4A). Moreover, DDX1 and RTCB's RNA-binding activities are enhanced in SINV and SARS-CoV-2 infected cells (Figure 4SA) (Garcia-Moreno et al., 2019; Kamel et al., 2021). We also noticed an enrichment of DDX1 and FAM98A in the cytoplasm of SINV-infected cells (Figure S4A and Table 5), and RTCB, DDX1 and FAM98A accumulate in SINV (Figure S4B). Collectively, these multiple lines of evidence ranked the tRNA-LC amongst the top five complexes with regulatory potential (Figure 4A).

To gain more insights into the role of the tRNA-LC in SINV life cycle, we tested if the complex remains unaltered after infection. We used a dox-inducible cell line expressing GFP-tagged FAM98A as bait or unfused GFP as negative control, and immunoprecipitated (IP) the complex using a nanobody against GFP. GFP-tagged proteins were noticeably enriched in IP eluates, while the abundant β-actin was missing (Figure 4B). Proteomic analysis of the eluates from SINV-infected cells shows FAM98A interacts with 608 (169 with 1% FDR plus an additional 439 with 10% FDR, Table 7), including the core components of tRNA-LC (DDX1, RTCB and CGI-99/C14orf166) and four viral proteins (capsid, nsP1, nsP2 and nsP3) (Figure 4C). Importantly, DDX1 and RTCB were within the top third quantile of FAM98A interactome (Figure 4D), suggesting near stoichiometric binding between these proteins also during SINV infection. Given the high abundance of viral proteins in infected cells, we normalised their intensity in eluates to those in the whole cell lysate, revealing that nsP1 is the primary interactor of the tRNA-LC (Figure 4E). NsP1 mediates the capping viral RNA and associate to membranes at the viral factories. A recent CryoEM structure showed that nsP1 forms a ring-like structure that is proposed to possess a 'gate keeper' role ensuring the release of processed vRNA (Jones et al., 2021). These results are consistent with the redistribution of tRNA-LC to viral

replication factories upon SINV infection (Garcia-Moreno et al., 2019). The tRNA-LC component DDX1 was also reported to interact with viral RNA capping enzyme in coronaviruses (nsP14) (Xu et al., 2010), despite the lack of homology between coronavirus and alphavirus proteins. Additionally, the tRNA-LC member CIG-99 (also hCLE) has been shown to interact with the cap structure (Pazo et al., 2019).

Next, we investigated whether the interactors of the tRNA-LC (FAM98A IP) are remodelled after infection. Indeed, 272 and 75 proteins were significantly enriched in mock and SINV infected cells, respectively, while the core components of tRNA-LC remained unaltered (Figure 4F, Table 8). GO analysis revealed that the tRNA-LC engages more prominently with splicing factors in mock cells, whereas rRNA processing and viral mRNA translation factors become prevalent in SINV-infected cells (Figure 4G and H). This switch from splicing to translation related machineries suggest a change of function for the tRNA-LC, which is supported by its subcellular redistribution after infection.

To test the relevance of the tRNA-LC in SINV infection, we established HEK293 lines inducibly expressing shRNAs targeting FAM98A and DDX1 (Figure S4C and D). DDX1 knockdown (KD) strongly reduced the amounts of intracellular vRNA and capsid protein. DDX1 KD also caused a profound reduction of extracellular gRNA, which corresponds to the viral progeny (Figure 5A and B). By contrast, FAM98A KD had minor or no effect on viral gene expression (Figure 5A). These contrasting results are associated with a reduction in the abundance of all the other components of the tRNA-LC, including the ligase RTCB, upon DDX1 KD that is not observed with FAM98A KD (Figure S4C). This loss of tRNA-LC components in absence of DDX1 is not due to a decrease in the levels of their cognate mRNAs (Figure S4D). DDX1-dependent disruption of the tRNA-LC was already observed in A549-ACE2 cells and suggests that DDX1 is essential for the assembly and stability of the tRNA-LC complex, while FAM98A may play a non-essential, secondary role (Kamel et al., 2021). The differential effect between DDX1 and FAM98A KDs in viral replication was also observed for SARS-CoV-2 (Kamel et al., 2021). To determine if DDX1 helicase activity is required for the observed phenotype, we expressed a dominant negative version of DDX1 with a mutation in the ATPase domain (K52A). $DDX1_{K52A}$-eGFP expression partially replaced the endogenous DDX1, further supporting the idea that the tRNA-

LC components must be present in a particular stoichiometry to be stable (Figure S4E). Expression of $DDX1_{K52A}$-eGFP induced a partial reduction in the levels of capsid in SINV-infected cells, highlighting the importance of DDX1 helicase activity in SINV infection (Figure S4C).

We next aimed to gather deeper insights into the effects of the tRNA-LC in SINV transcriptome and performed an RNA sequencing (seq) analysis in SINV-infected DDX1 KD cells. Notably, SINV RNAs were amongst the most significantly downregulated transcripts upon DDX1 KD when compared to uninduced cells, together with *ddx1* mRNA itself (Figure 5C). To test if the roles of the tRNA-LC are linked to viral replication, we determined the amount of reads mapping to the positive and negative vRNA strands. Strikingly, DDX1 KD affected to the same extent the negative and positive genomic (g)RNA strands (Figure 5D and S5A). Synthesis of the negative strand occurs mainly during the first few hours after infection (Strauss and Strauss, 1994), posing that the tRNA-LC likely participates in the initial steps of the viral life cycle, either supporting viral replication and/or the translation of the genomic RNA to produce the RdRp complex. To test if also transcription of the subgenomic (sg)RNA is affected, we estimated the ratio between the reads mapping to the genomic gRNA and to the gRNA/sgRNA overlap (Figure S2K). DDX1 KD did not affect the gRNA/sgRNA ratio (Figure 5E), suggesting that tRNA-LC does not contribute to sgRNA transcription. Additionally, we did not notice a higher incidence of mismatches in the reads mapping to SINV RNA (i.e. mutations), which implies that tRNA-LC disruption does not affect the fidelity of the RdRp.

We next asked if the tRNA-LC specifically regulates SINV or instead has a broader role in alphavirus infection. To test this, we monitored the infection of SINV-mCherry, SFV-mCherry and RRV-mCherry upon DDX1 KD and observed that the loss of the tRNA-LC had a strong effect in the fitness of these three viruses (Figure 5G), invoking a central role in alphavirus infection.

In a parallel work we showed that DDX1 KD also hampers SARS-CoV-2 infection (Kamel et al., 2021). To assess to what extent the role of tRNA-LC in SARS-CoV-2 infection is similar to SINV, we analysed RNA-seq data from A549-ACE2 DDX1 KD cells infected with SARS-CoV-2. In agreement to SINV, both positive and negative sense RNAs of SARS-CoV-2 were severely reduced by DDX1 KD (Figure S5A and

B). Collectively, these results show that the tRNA-LC has wide spread regulatory roles in virus replication, although its exact mechanism of action awaits to be deciphered.

SINV RNP components hold potential as therapeutic targets

The tRNA-LC illustrates the power of vRIC at identifying key regulators of the viral life cycle. However, this example is likely to be the tip of the iceberg. To assess the incidence of regulators of the viral life cycle within SINV RNP components, we performed a metanalysis of 73 genome-wide screenings focused on the discovery of relevant host-virus interactions. The screens were performed using different strategies (i.e. siRNA, CRISPR/cas9) and a wide range of viruses (36 viruses from 18 families; Figure S6A-B). The overlap between these datasets is, however, limited (Figure S6C), which is expected because of the broad range of approaches and viruses used as well as the noticeable incidence of false positives and negatives associated to genome wide screenings. Strikingly, SINV RNP components are supported as host-virus interactors by significantly higher number of screens, on average, than proteins enriched in cRNPs (Figure 6A). Because *bona fide* regulators of virus infection are expected to be present in several independent screens, we compiled the proteins whose involvement in infection is supported by at least three screens, while considering 'master regulators' those spanning three or more virus families. Importantly, SINV RNPs are significantly more enriched in both 'potential regulators' and 'master regulators' when compared to proteins enriched in cRNP (Figure 2B and 6B). Together, these results confirm that SINV RNPs are enriched in cellular factors with regulatory roles in virus infection.

We reasoned that if the vRNP composition is critical for virus infection, then cellular proteins that interact with vRNA should be inherently enriched in potential targets for antiviral therapies. To test this hypothesis, we identified the RBPs within SINV RNPs with available inhibitors, and found 23 putative 'therapeutic targets' with 124 verified inhibitors (Figure S6D). Out of these, we selected two classes of compounds: the first-class targets RBPs with domains involved in nucleic acid processing and modification, such as 5-Azacytidine that inhibits 5-methylcytosine (m^5C) methyltranferases (DNMT1 and NOP2/NSUN1) and Topotecan that do so with topoisomerase I (TOP1). The second class targets kinases that can potentially modulate the vRNP microenvironment, which included PF-480056 and PF-3758309 that inhibit CSNK1E

and PAK4, respectively. We tested the effects of these inhibitors in the viral fitness of SINV-mCherry, SFV-mCherry and RRV-mCherry. 5-Azacytidine (cytosine methyltransferases inhibitor) and Topotecan (TOP1 inhibitor) inhibited the infection of these three alphaviruses in a dose-dependent manner, strongly reducing viral RNA and proteins (Figure 6C-E). Moreover, we also noticed a dose-dependent decrease of vRNA in the supernatant of infected cells, which implies reduction in viral particle production (Figure 6F). These strong inhibitory effects were not associated with viability defects due to toxicity (Figure S6E). On the other hand, CSNK1E (PF-480056) and PAK4 (PF-3758309) inhibitors had only mild antiviral effects on SINV fitness, with no apparent effect in the other alphaviruses (Figure 6H-I and S6F-G).

Given the strong effects of 5-Azacytidine and Topotecan in alphavirus infection, we explored if these compounds also have effects in the infection of other viruses from different families, particularly human immunodeficiency virus type 1 (HIV-1, *Retroviridae*) and coxsackievirus B3 (CVB3, *Picornaviridae*). Using chimeric HIV-1$_{\text{-R-E-mCherry-Nef}}$ replicon (Garcia-Moreno et al., 2019) and CVB3$_{\text{eGFP}}$ (Lanke et al., 2009), we observed that 5-Azacytidine and Topotecan also inhibits gene expression of these unrelated RNA viruses (Figure 6G). Importantly, Topotecan and 5-Azacytidine are clinically approved drugs used in cancer treatment (Blagosklonny, 2004; Kaminskas et al., 2005), and our results highlight them as potential broad-spectrum antivirals.

OUTLOOK

vRNA has emerged as a hub for critical host-virus interactions. We provide a systematic and comprehensive approach, vRIC, to elucidate the composition of vRNPs in infected cells. In its present form, vRIC can be applied to study any polyadenylated vRNA. Exchange of oligo(dT) by specific antisense probes or total RNA isolation methods (Iselin et al., 2021) can expand the reach of vRIC to a wide range of RNA and DNA viruses encoding an RdRp. In the present work we have applied vRIC to study SINV RNPs, revealing over 400 cellular proteins that interact with vRNA. These proteins range from well-characterised classical RBPs involved in splicing, RNA export, stability, and translation, to unorthodox RBPs with no known or poorly characterised RBDs. These unorthodox RBPs include kinases, E3 ubiquitin ligases, chaperones, and metabolic enzymes that may regulate the RNP microenvironment. Here, we applied vRIC to a single time post infection, and we

foresee that the use of vRIC at different time points will shed light on the host-virus interactions driving the different stages of the viral life cycle.

A highlight of this study is that vRNA may act as a 'spiderweb' that captures nuclear RBPs in the cytoplasm of the infected cell defining the composition of vRNPs. Our protein-protein interaction study with FAM98A revealed that the tRNA-LC interacts with the spliceosome primarily in uninfected cells and switches to the translation apparatus in infected cells, correlating with the relocation of this complex to the viral replication factories. This raises the idea that changes in the location and, consequently, molecular partners of RBPs may cause a functional repurposing in infected cells. Such exciting possibility should be further explored in the future.

vRIC highlights the tRNA-LC as a master regulator of RNA virus infection that controls the replication of several alphaviruses (present work) and SARS-CoV-2 (Kamel et al., 2021). Future studies should be undertaken to decipher the mechanism by which the tRNA-LC regulates the life cycle of these viruses. The tRNA-LC is just the tip of the iceberg and vRNPs are enriched in regulatory RBPs. Our dataset contains 23 therapeutic targets with more than 100 inhibitors available. Future work should test whether these compounds have antiviral effects and can be used in new therapies. The potential of the identified RBPs is illustrated by 5-Azacytidine and Topotecan, which inhibit the infection of three different alphaviruses (SINV, SFV and RRV), CVB3 and HIV-1 in cultured cells. The utility of these drugs as antivirals should be explored in the future.

ACKNOWLEDGEMENTS

A.C. is supported by a Medical Research Council (MRC) Career Development Award MR/L019434/1, MRC grants MR/R021562/1, MC_UU_12014/10, and MC_UU_12014/12. W.K. is funded by the European Union's Horizon 2020 research and innovation programme under Marie-Sklodowska-Curie n# 842067. V.R. is funded by the European Union's Horizon 2020 research and innovation programme under Marie-Sklodowska-Curie n#892756. L.I. is funded by the BBSRC DTP scholarship number BB/M011224/1. N.P. is funded by the MRC CVR PhD programme. J.M. is funded by the Medical University of Vienna, and the "Fonds zur Förderung der wissenschaftlichen Forschung (FWF)" as Stand-Alone Project P29888. I.D. is funded

by the Wellcome Investigator Award 209412/Z/17/Z and Wellcome Strategic Awards 091911/B/10/Z and 107457/Z/15/Z. We thank Luis Carrasco and Miguel A Sanz for de critical reading of the manuscript. We thank F. J. M. van Kuppeveldd for the CVB3-eGFP construct.

AUTHOR CONTRIBUTIONS

Conceptualization, W.K., S.M.[2], A.C.; Methodology, W.K., L.I., N.P., A.I.J. S.M.[2], A.C.; Investigation, W.K., V.R., L.I., N.P., M.G.M., S.M.[1], A.I.J., M.H., S.M.[2], A.C.; Writing, original draft, W.K., S.M.[2] and A.C.; Writing, editing, W.K. V.R., L.I., N.P., M.G.M., A.I.J., M.H., A.M., J.M., S.M., A.C.; Funding acquisition, W.K., S.M.[2], A.C.; Resources, A.M., J.M., S.M.[2], A.C.; Supervision, W.K., S.M.[2], A.C.

MATERIALS AND METHODS

Experimental model and subject detail

Cell culture

HEK293 cells were maintained in DMEM (Gibco, 41965039) with 10% fetal bovine serum (FBS) (Gibco, 10500064) and 1x penicillin/streptomycin (Sigma Aldrich, P4458) at 37°C with 5% CO_2. BHK21 and HEK293T cells, for growing virus stocks, were maintained in same conditions.

Viruses

Alphaviruses used were Sindbis virus that was produced by in vitro transcription from the plasmid pT7svwt (Castello et al., 2006). Replicative alphaviruses with fluorescent reporters (SINV-mCherry and SFV-mCherry) were generated by duplication of subgenomic promoter and insertion of mCherry (Garcia-Moreno et al., 2019). For RRV-mCherry, the mCherry sequence was inserted after a duplicated subgenomic promoter placed between the non-structural and structural proteins (unpublished). Coxsackie B3 virus (CVB3) has eGFP inserted at the N-terminus followed by a 3Cpro cleavage site at N-terminus (Lanke et al., 2009). From retroviruses, we used HIV-1 replicon mCherry tagged (pNL4-3.R-E-Nef-mCherry).

Viral RNA interactome capture

HEK293 cells were grown in sets of 4x15 cm dishes. Cells were infected with SINV for 1h with a multiplicity of infection (MOI=1). After 1h, supernatant was replaced with fresh media supplemented with 20 μM Flavopiridol hydrochloride hydrate (Fvo, Cat.No. F3055, Sigma-Aldrich) and incubated at 37°C for 2 hours. At 3hpi, the supernatant was replaced with fresh media supplemented with 20 μM Flavopiridol hydrochloride hydrate (Fvo, Cat.No. F3055, Sigma-Aldrich) and 100 μM 4-Thiouridine (4SU, Cat.No. T4509, Sigma-Aldrich), an incubated at 37°C. At 24hpi, media was discarded, and cells were rinsed once with PBS (Phosphate-buffered saline). After removal of the PBS, the cell monolayer was irradiated twice with 200 mJ/cm2 using ultraviolet light at 365nm. At this stage, cells were lysed and polyadenylated RNA purified with oligo(dT) magnetic beads as in (Castello et al., 2013; Garcia-Moreno et al., 2019). Briefly, cells pellets were lysed with 8 mL of lysis buffer (20 mM Tris-HCl pH 7.5, 500 mM LiCl, 0.5% LiDS wt/vol, 1 mM EDTA, 0.1% IGEPAL (NP-40) and 5 mM DTT). This is followed by lysate homogenization, which is performed by pressing the lysate through 5 mL syringe equipped with 27G needle repeatedly until the lysates is no longer viscous. Then homogenized lysate incubated with 0.80 mL of pre-equilibrated oligo(dT)25 magnetic beads (New England Biolabs, #S1419S) for 1 h at 4°C with gentle rotation. Beads were collected by magnet and the lysate was transferred to a new tube and stored at 4°C. Beads were washed once with 5 mL of lysis buffer, followed by two washes with 5 mL of buffer 1 (20 mM Tris-HCl pH 7.5, 500 mM LiCl, 0.1% LiDS wt/vol, 1 mM EDTA, 0.1% IGEPAL and 5 mM DTT), and two washes with buffer 2 (20 mM Tris-HCl pH 7.5, 500 mM LiCl, 1 mM EDTA, 0.01% IGEPAL and 5 mM DTT), in all washes the beads were incubated for 5 min at 4°C with gentle rotation. Beads were then washed twice with 5 mL of buffer 3 (20 mM Tris-HCl pH 7.5, 200 mM LiCl, 1 mM EDTA and 5 mM DTT) at room temperature for 3 minutes. Beads were resuspended in 300 μL of elution buffer and incubated for 3 min at 55°C with agitation. After collecting the beads with a magnet, eluates (supernatants) were collected and stored at −80°C. The lysates were subjected to a second round of capture and the eluates from the first and second cycles were combined. Prior to mass spectrometry sample processing, samples were RNase treated with ~0.02U RNase A and RNase T1 at 37°C for 1h. The controls described in Figure 1B were generated as above but virus, Fvo or/and UV irradiation were omitted.

Subcellular fractionation

HEK293 cells ($4X10^6$) were infected with SINV (10 MOI) or mock-infected for 24 hours. To separate the cytoplasmic and nuclear fractions, cells were harvested and suspended in 1X PBS, followed by centrifugation at 600 xg for 5 min at 4°C, the cell pellet was incubated with 500 µL lysis buffer (1% IGEPAL, 150 mM NaCl, 50mM HEPES pH 7.9, 0.1 mM AEBSF serine protease inhibitor) at 4°C for 10 mins. Followed by centrifugation at 7000g for 5min, the cytoplasmic supernatant was transferred to new tube and cleared by centrifugation at 15,000g at 4°C for 5 min. The pellet (nuclear fraction) was suspended in 500µL RIPA buffer (0.1%SDS, 0.5% sodium deoxycholate, 150 mM NaCl, and 50mM HEPES, pH 7.9 and 0.1 mM AEBSF serine protease inhibitor) supplemented with Benzonase (1 µL/mL) and incubated on ice for 1 hour. Next, Nuclear lysate was boiled for 2 min and cleared by centrifugation at 15,000g for 5 min. For proteomic analysis four biological replicates were created.

Protein-protein interaction analysis

$4.5x10^6$ HEK293 FlpIn/TRex expressing eGFP or FAM98A-eGFP were induced with 1 µg/mL doxycycline for 24h. Next, cells were infected with SINV(MOI=10) in FBS-free DMEM and incubated for 1h, control cells were mock-infected. Subsequently, media was exchanged with 10% FBS-containing DMEM and incubated for 18h. Cells were collected and lysed in 1 mL lysis buffer (10 mM Tris/HCl pH 7.5, 150 mM NaCl, 0.5 mM EDTA, 0.5 % Nonidet™ P40 Substitute, 0.1 mM AEBSF serine protease inhibitor) containing 1 µL/mL Benzonase (Millipore, #70746-4). 25 µL of GFP_Trap agarose beads were equilibrated in lysis buffer and incubated with the whole cell lysate for 2h at 4°C with gentle rotation. Beads were washed four times with 500 µL lysis buffer. An additional wash step was performed with 500 µL of wash buffer (10 mM Tris/HCl pH 7.5, 150 mM NaCl, 0.5 mM EDTA, 0.1 mM AEBSF serine protease inhibitor) and proteins were eluted twice with 50 µL glycine-elution buffer (200 mM glycine pH 2.5) neutralized with 15 µL neutralization buffer (1 M Tris pH 10.4). Two biological replicates were used for the proteomic experiment.

Cell lysis and Western blot

To prepare whole cell lysate for western blotting, virus- and mock-infected cells were harvested at the times indicated in the figures, washed once with 1X PBS and resuspended in RIPA buffer 0.1% SDS, 0.5% sodium deoxycholate, 150 mM NaCl, and 50mM HEPES, pH 7.9 and 0.1 mM AEBSF serine protease inhibitor) supplemented with Benzonase (1 µl/ml) and incubated on ice for 1 hour. Next, total lysate was boiled for 2 min and cleared by centrifugation at 15,000g for 5 min. Western blotting was performed as previously described in (Garcia-Moreno et al., 2019), antibodies used are listed in Table 9.

Immunofluorescence

$1.5x10^5$ HeLa FlpIn/TRex GFP, DDX1-GFP, RTCB-GFP or FAM98A-GFP cells were seeded on pre-washed High Precision Coverslips (Merienfeld, #0107052) and incubated in DMEM with 10% FBS supplemented with 1ug/ml doxycycline for 16 h. Subsequently, cells were either mock-infected or infected with SINV(MOI=10). At 18 hpi, cells were fixed and treated for immunofluorescence with α-SINV C antibody at 1:200 dilution and GFP-Booster_Atto488 (ChromoTek GmbH, #gba488-100) at 1:500 dilution following the procedure described in (Garcia-Moreno et al., 2019). Images were acquired on a Zeiss LSM880 with Airyscan, using a 63x oil Plan-Apochromat DIC M27 objective (NA 1.4).

RNA extraction and qRT-PCR

Cells were harvested at indicated time points, and centrifuged for 5 min at 600xg. Cell pellets were washed once with PBS and resuspended in TRIzol Reagent (ThermoFisher scientific). RNA was later chloroform-extracted and precipitated by isopropanol according to the manufacture instructions. RNA pellets were washed twice with 80% ethanol, and suspended in RNAse-free water. To purify extracellular RNA, media collected from infected cells and were mixed 1:3 (v/v) with TRIzol Reagent (ThermoFisher scientific) followed by chloroform extraction. This followed by RNA clean-up and concentration by RNA Clean & Concentrator™-25 kit (Zymo Research). Reverse transcription and qRT-PCR analysis was performed by Luna universal one-step qRT-PCR kit (NEB # E3005L) with primers list in Table 9.

DDX1 mutagenesis

The plasmid expressing DDX1-K52A was generated by site-directed mutagenesis using pcDNA5-FRT-TO-eGFP-DDX1 (Garcia-Moreno et al., 2019) as a template. Primers are listed in Table 9. The mutagenesis was confirmed by sequencing.

mCherry and GFP microplate reader assay

Briefly, $1x10^4$ HEK293 cells were seeded on each well of a 96-well microplate with flat mClear bottom (Greiner Bio-One, #655986) in DMEM media without phenol-red and supplemented with 10% FBS and 1 mM sodium pyruvate. For mCherry- and eGFP-tagged viruses, cells are infected at MOI=10 in in complete DMEM (lacking phenol-red) with 5% FBS. Cells were incubated at 37°C and 5% CO2 in a CLARIOstar fluorescence plate reader (BMG Labtech) for the indicated time periods. For GFP signal measurement assay, HEK293 FlpIn TRex GFP cells were induced with 1ug/ml doxycycline, prior to incubation in the microplate reader.

Drugs and cell viability

To test cell viability and proliferation at the concentrations used, we seeded $7.5x10^4$ HEK293 FlpIn/TRex cells in 200µL clear DMEM + 5% FBS + 1 mM sodium pyruvate per well of a 96-well microplate (flat, transparent bottom). 24 h later cells were treated with each stated compound and incubated for another 18 h at 37°C and 5%CO2. Cell viability was estimated by adding CellTiter 96 Aqueous One Solution (Promega, #G3580) and measuring 490 nm absorbance on a plate reader following the manufacturer's recommendations. In parallel, the number of cells was counted using the Countess II FL Automated Cell Counter (Thermo Fisher Scientific). Compounds are listed in Table 9.

Mass spectrometry

Proteins samples (vRIC ,PPI eluates, cytoplasmic and nuclear fractions lysates) were treated with benzonase (1 µL/mL) followed by clean-up via the bead-based single-pot, solid-phase-enhanced sample-preparation (SP3) method, using Magnetic Carboxylate Modified Particles beads (Sigma-Aldrich, cat.no.45152105050250). Protein digestion was performed on beads using Trypsin Gold (MS grade; Promega,

cat. no. V5280), as previously described in (Hughes et al., 2019). For processed peptides, liquid chromatography (LC) was performed using an Ultimate 3000 ultra-HPLC system (Thermo Fisher Scientific). Peptides were initially trapped in C18 PepMap100 pre-column (300 µm inner diameter x 5 mm, 100A, Thermo Fisher Scientific) in Solvent A (Formic acid 0.1% (v/v), Medronic acid 5 µM). Trapped Peptides were separated on the analytical column (75 µm inner diameter x 50cm packed with ReproSil-Pur 120 C18-AQ, 1.9 mm, 120 A, Dr. Maisch GmbH) in a 60min 15%–35% [vol/vol] acetonitrile gradient with constant 200 nL/min flow rate. Separated peptides were directly electrosprayed into a QExactive mass spectrometer (Thermo Fisher Scientific). Mass spectra were acquired in the Orbitrap (scan range 350-1500 m/z, resolution 70000, AGC target 3 x 10^6, maximum injection time 50 ms) in a data-dependent mode. the top 10 most abundant peaks were fragmented using CID (resolution 17500, AGC target 5 x10^4, maximum injection time 120 ms) with first fixed mass at 180 m/z.

Proteomic quantitative analysis

Protein identification and quantification were performed using Andromeda search engine implemented in MaxQuant (1.6.3.4) under default parameters (Cox et al., 2011). Peptides were searched against reference Uniport datasets: human proteome (Uniprot_id: UP000005640, downloaded Nov2016) and SINV proteome derived from pT7-SVwt plasmid. False discovery rate (FDR) was set at 1% for both peptide and protein identification. MaxQuant search was performed with “match between run” only activated in the search of cytoplasmic and nuclear fractions samples.

MaxQuant (proteinGroups) outputs were used for downstream relative quantification. Proteins flagged as potential contaminants by MaxQuant were filtered out, R-package “DEP (1.4.1)”, together with proteins with missing values across all samples. For relative quantification between Mock or infected samples, proteins raw intensities were normalized, within the same cellular fraction (in case of the fractionation experiment) or same bait (in FAM98A-GFP PPI experiments), and transformed using R-package Variance Stabilizing Normalization “VSN (3.50.0)”. Missing value imputation was performed for proteins undetected in all replicates in one experimental condition, while present in the other condition (at least in 2 replicates). Imputation was implemented using local minimum determination method (Mindet) (Lazar et al., 2016). R-package

“limma (3.38.3)” were used for statistical analysis for the processed protein intensities applying the empirical Bayesian method moderated t-test with p-values adjusted for multiple-testing using Benjamini-Hochberg method. For the vRIC samples, protein intensities were processed as described above but omitting the normalization step.

Analysis of RBP binding preferences with ENCODE eCLIP data

eCLIP bed files were downloaded from the ENCODE database use ENCODExplorer on 07/04/21. GRCh38.99 reference genome annotation from ensemble (ftp://ftp.ensembl.org/pub/release-99/gtf/homo_sapiens/Homo_sapiens.GRCh38.99.chr.gtf.gz) was used to determine the features within which binding sites occurred. This was achieved using the findOverlaps function from the genomicRanges package to align coordinates of eCLIP hits with genome annotations. To identify eCLIP hits present in introns, an intron annotation object was created by extracting the coordinates between exons of genes from the genome annotation. This was then used in the same way as the genome annotation to identify overlap with eCLIP hits. To determine the proportion of binding sites occurring within each feature, binding sites were filtered to include only those occurring in protein coding genes and counted. The frequency of binding sites in each feature was converted to a proportion of total number of binding sites in protein coding genes. 'Binding preference' was assigned based on the feature with the highest proportion of binding sites.

Drug-protein interactions

In order to identify potential inhibitor for vRNPs, we mined known chemical compound interactions available through the Drug-Gene Interaction database (DGIdb, downloaded Oct-2020) (Cotto et al., 2018), and selected interactions with inhibitory mode of action (reported as "inhibitor”).

Intrinsically disordered regions and Pfam RNA-binding domains analysis

Prediction of intrinsically disordered regions were obtained from MobiDB done by MobiDB-lite method (Piovesan et al., 2021). Assigning RNA binding proteins with either classical or non-classical domains was performed as previously described in (Kamel et al., 2021).

Protein Complexes enrichment analysis

To identify known RNP complex bound to viral RNA, list of curated human complexes obtained from CORUM database (Giurgiu et al., 2019). Complexes with less than 3 verified RBPs, based on RBPbase, were filtered out. The remaining complexes were selected to contain at least one RBP with increased poly(A)RNA binding during SINV infection (Garcia-Moreno et al., 2019). This was followed by the estimation of the percentage of the components of RBP complexes present in SINV RNPs.

RNA sequencing analysis

To assess the effect of DDX1 on SINV infection, $0.8x10^6$ HEK293 inducible-shDDX1 cells were seeded on a 6 well plate with 10% FBS-containing DMEM supplemented with 1 µg/ml doxycycline, or without doxycycline as control, and incubated for 56 h. Cells were either Mock-infected or infected with SINV-mCherry (MOI 0.1) for 18 hours, followed by RNA extraction. RNA-seq samples processing, library preparation and differential gene expression analysis were performed as previously described in (Kamel et al., 2021). For the analysis of viral RNA, in order to estimate the gRNA to sgRNA ratio, mapped reads up to the 7600nt (upstream of the subgenomic promoter) are assigned as gRNA reads and downstream reads assigned as sgRNA reads for simplicity. In order to assess the effect of DDX1 on accumulation of SARS-CoV2 positive and negative strands, previously deposited data were used (GEO: GSE171382).

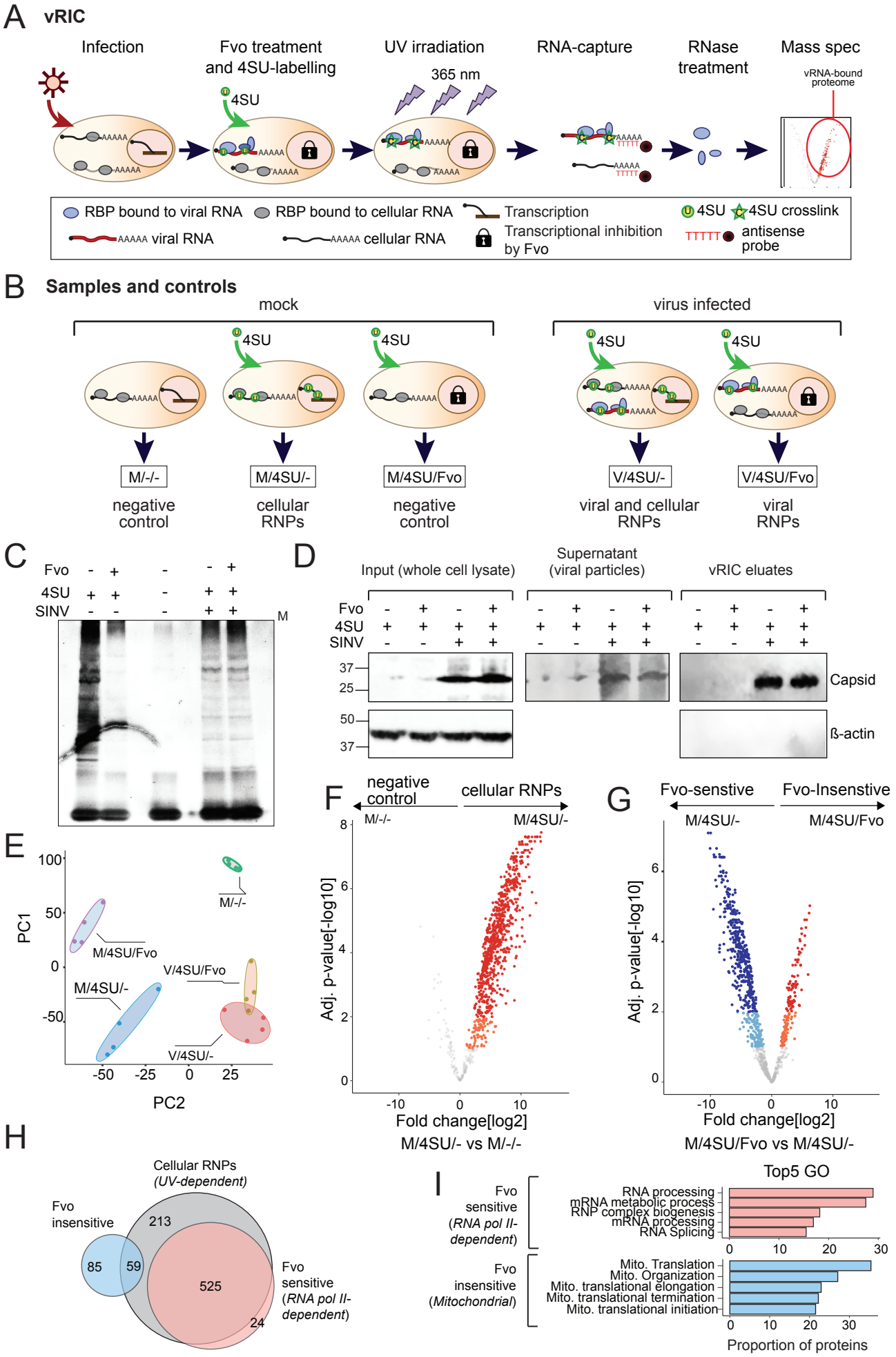
A vRIC
Infection
Fvo treatment and 4SU-labelling
UV irradiation
365 nm
RNA-capture
RNase treatment
Mass spec
vRNA-bound proteome
4SU
RBP bound to viral RNA
RBP bound to cellular RNA
Transcription
Transcriptional inhibition by Fvo
4SU crosslink
viral RNA
cellular RNA
antisense probe
B Samples and controls
mock
virus infected
M/-/-
M/4SU/-
M/4SU/Fvo
V/4SU/-
V/4SU/Fvo
negative control
cellular RNPs
negative control
viral and cellular RNPs
viral RNPs
C
Fvo
4SU
SINV
M
D
Input (whole cell lysate)
Supernatant (viral particles)
vRIC eluates
Capsid
ß-actin
E
PC1
PC2
M/-/-
M/4SU/Fvo
M/4SU/-
V/4SU/Fvo
V/4SU/-
F
negative control
cellular RNPs
M/-/-
M/4SU/-
Adj. p-value[-log10]
Fold change[log2]
M/4SU/- vs M/-/-
G
Fvo-senstive
Fvo-Insenstive
M/4SU/-
M/4SU/Fvo
Adj. p-value[-log10]
Fold change[log2]
M/4SU/Fvo vs M/4SU/-
H
Cellular RNPs (UV-dependent)
Fvo insensitive
Fvo sensitive (RNA pol II-dependent)
213
85
59
525
24
I
Top5 GO
Fvo sensitive (RNA pol II-dependent)
RNA processing
mRNA metabolic process
RNP complex biogenesis
mRNA processing
RNA Splicing
Fvo insensitive (Mitochondrial)
Mito. Translation
Mito. Organization
Mito. translational elongation
Mito. translational termination
Mito. translational initiation
Proportion of proteins

Figure 1

Figure 1. vRIC implementation in SINV infected cells.

A) Schematic of the viral RNA interactome capture (vRIC) workflow.

B) Schematic of the different experimental conditions and controls used in the study.

C) Sliver staining analysis of vRIC eluates with the experimental setting outlined in B.

D) Immunoblotting of SINV capsid in whole cell lysates, supernatant and vRIC eluates, using β-actin as control.

E) Principal component analysis of vRIC experimental and controls after proteomic analysis.

F and G) Volcano plots showing the fold change(log_2) and adjusted p-value of each protein (dot) in the M/-/- versus M/4SU/- (F) and M/4SU/- versus M/4SU/Fvo (G) comparisons. Proteins enriched within 1% FDR are coloured in red and blue and those within 10% FDR in orange and cyan.

H) Venn diagram comparing the proteins significantly enriched in each of the comparisons in F-G. These groups are classified: UV-dependent RBPome (M/-/- vs M/4SU/-), Fvo-sensitive (enriched in M/4SU/- over M/4SU/Fvo, cRNPs) and Fvo-insensitive (enriched in M/4SU/Fvo over M/4SU/-, mitoRNPs).

I) Top enriched Gene Ontology (GO) terms for Molecular processes in Fvo-sensitive and Fvo-insensitive RBP sets.

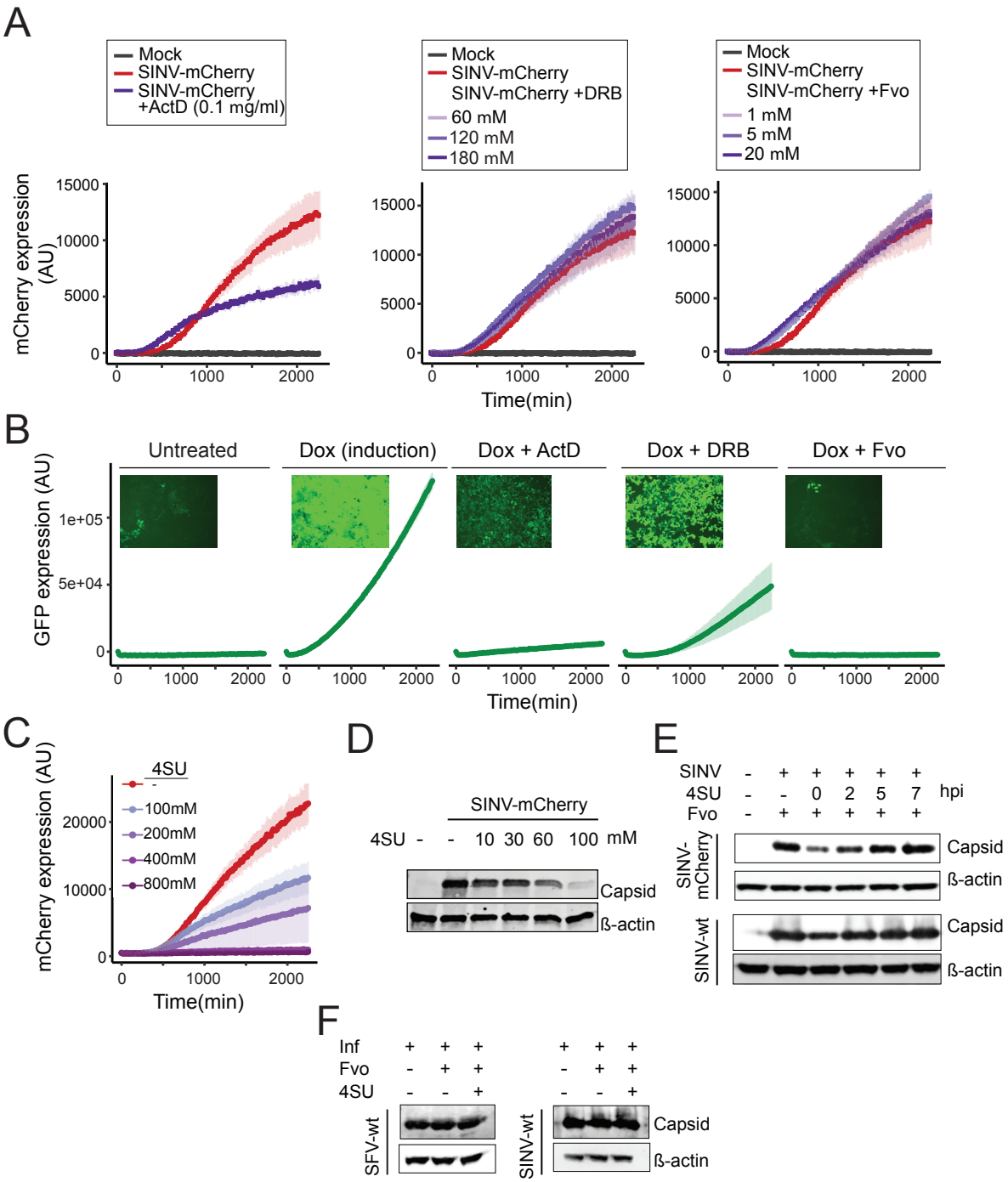
A
Mock
SINV-mCherry
SINV-mCherry +ActD (0.1 mg/ml)
SINV-mCherry +DRB
60 mM
120 mM
180 mM
SINV-mCherry +Fvo
1 mM
5 mM
20 mM
mCherry expression (AU)
Time(min)
B
Untreated
Dox (induction)
Dox + ActD
Dox + DRB
Dox + Fvo
GFP expression (AU)
Time(min)
C
4SU
100mM
200mM
400mM
800mM
mCherry expression (AU)
Time(min)
D
SINV-mCherry
4SU - - 10 30 60 100 mM
Capsid
ß-actin
E
SINV - + + + + +
4SU - - 0 2 5 7 hpi
Fvo - + + + + +
SINV-mCherry
SINV-wt
Capsid
ß-actin
F
Inf + + + + + +
Fvo - + + - + +
4SU - - + - - +
SFV-wt
SINV-wt
Capsid
ß-actin

Figure S1

Figure S1. Optimisation of the vRIC experiment.

A) Graph showing red fluorescent signal derived from SINV-mCherry infected cells treated with different RNA polymerase II inhibitors at different concentrations, Actinomycin D (ActD), 5,6-dichloro-1-β-D-ribofuranosyl benzimidazole (DRB) and Flavopiridol (Fvo). Fluorescence was measured every 15 min over a period of 36 h.

B) Graph showing the green fluorescence derived from GFP produced after addition of deoxicycline to cultured HEK293 eGFP and in presence of the different inhibitors of RNAPs described in (A). Measurement was performed as in A.

C) SINV-mCherry derived fluorescent signal in cells treated with different doses of 4SU. Measurements were performed as in (A). A-C) Error bars indicate standard deviation, n=3.

D-E) Immunoblot of SINV capsid and β-actin from mock and infected cells upon treatment C) with increasing concentrations of 4SU or D) with a fix dose of 4SU added at different hpi. E) Immunoblot of capsid in cells infected with SINV or SFV and treated or not with 4SU and Fvo 2h after infection. hpi, hour post infection.

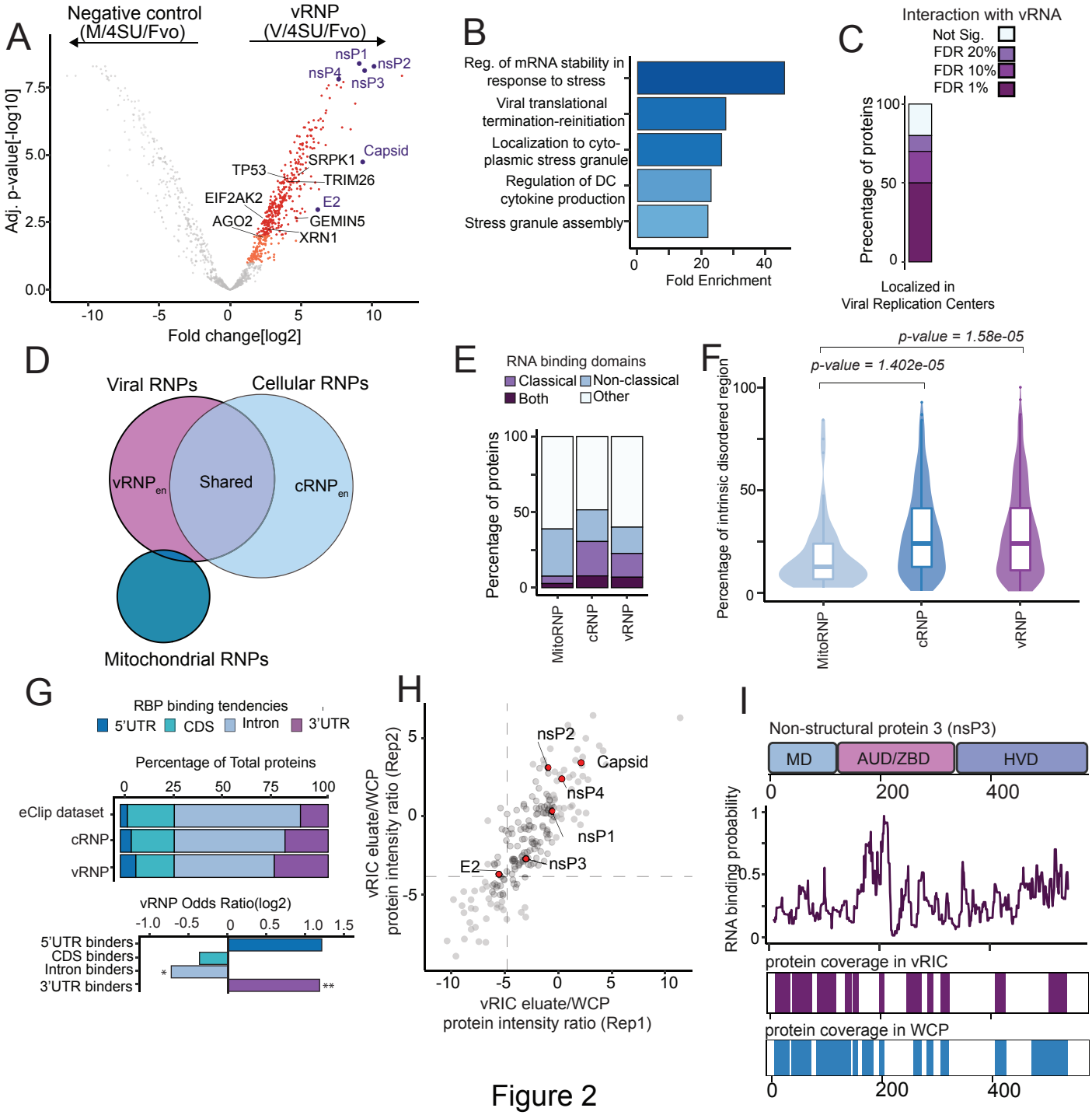
A
Negative control (M/4SU/Fvo)
vRNP (V/4SU/Fvo)
nsP1
nsP2
nsP4
nsP3
Capsid
SRPK1
TP53
TRIM26
EIF2AK2
E2
AGO2
GEMIN5
XRN1
Adj. p-value[-log10]
Fold change[log2]
B
Reg. of mRNA stability in response to stress
Viral translational termination-reinitiation
Localization to cyto-plasmic stress granule
Regulation of DC cytokine production
Stress granule assembly
Fold Enrichment
C
Interaction with vRNA
Not Sig.
FDR 20%
FDR 10%
FDR 1%
Precentage of proteins
Localized in Viral Replication Centers
D
Viral RNPs
Cellular RNPs
vRNP en
Shared
cRNP en
Mitochondrial RNPs
E
RNA binding domains
Classical
Non-classical
Both
Other
Percentage of proteins
MitoRNP
cRNP
vRNP
F
p-value = 1.58e-05
p-value = 1.402e-05
Percentage of intrinsic disordered region
MitoRNP
cRNP
vRNP
G
RBP binding tendencies
5'UTR
CDS
Intron
3'UTR
Percentage of Total proteins
eClip dataset
cRNP
vRNP
vRNP Odds Ratio(log2)
5'UTR binders
CDS binders
Intron binders
3'UTR binders
H
nsP2
Capsid
nsP4
nsP1
E2
nsP3
vRIC eluate/WCP protein intensity ratio (Rep2)
vRIC eluate/WCP protein intensity ratio (Rep1)
I
Non-structural protein 3 (nsP3)
MD
AUD/ZBD
HVD
RNA binding probability
protein coverage in vRIC
protein coverage in WCP

Figure 2

Figure 2. Uncovering the composition of SINV RNPs.

A) Volcano plot showing fold change and adjusted p-value for each protein (dot) in the comparison between M/4SU/Fvo versus V/4SU/Fvo. Proteins enriched within 1% FDR are coloured in red and those within 10% FDR in orange. Proteins significantly enriched in the V/4SU/Fvo are classified as SINV RNP components.

B) Bar plot showing the most enriched 'biological process' GO terms for vRNPs.

C) Bar plot indicating the percentage of proteins colocalised in SINV viral factories using the limited localisation screen in Garcia-Moreno et al., 2019, that are classified as SINV RNP components by vRIC at different FDR cut-offs (FDR < 20, 10 and 1%).

D) Venn diagram comparing the set of RBPs within vRNPs, cRNPs and mitoRNPs.

E) Bar plot defining the proportion of RBPs with classical, nonclassical, both or undefined RBDs in components of vRNPs, cRNPs and mitoRNPs.

F) Prevalence of intrinsic disorder regions (IDRs) in vRNPs, cRNPs and mitoRNPs. p-values were estimated by Welch's t-test.

G) Upper panel, bar plot showing the proportion of RBPs with biases towards 5' UTR, 3' UTR, CDS and introns in vRNPs, cRNPs and the whole ENCODE eCLIP superset. Lower panel, Enrichment or depletion of RBPs with preferences for intron, 5' and 3'UTR binders in vRNPs over cRNPs. *, $p < 0.1$ and **, $p < 0.05$ estimated by Fisher's Exact test.

H) Scatter plot showing the protein intensities ratios in vRIC eluate over whole cell proteome (WCP) in two biological replicates. Viral proteins detected by vRIC are highlighted.

I) Upper panel, domain architecture of nsP3 (the macro domain (MD), alphavirus-unique or zinc-binding domain (AUD/ZBD) and hypervariable domain (HVD)). Middle panel, profile showing the probability for RNA binding at every amino acid of nsP3. Lower panels, position of the peptides identified in vRIC eluates and WCP.

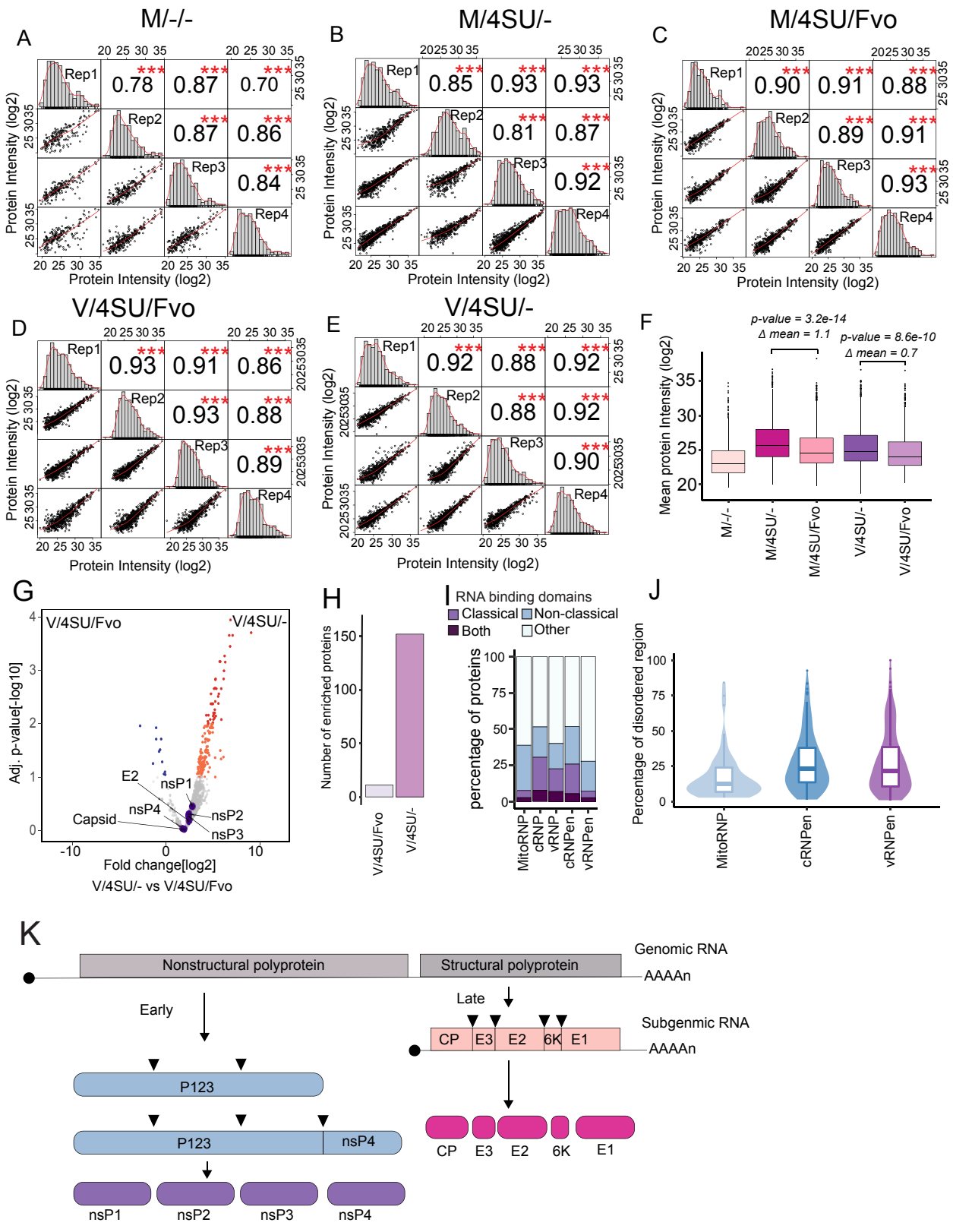
A
M/-/-
B
M/4SU/-
C
M/4SU/Fvo
D
V/4SU/Fvo
E
V/4SU/-
Rep1
Rep2
Rep3
Rep4
0.78
0.87
0.70
0.87
0.86
0.84
0.85
0.93
0.93
0.81
0.87
0.92
0.90
0.91
0.88
0.89
0.93
0.91
0.86
0.93
0.88
0.89
0.92
0.88
0.92
0.88
0.92
0.90
Protein Intensity (log2)
F
p-value = 3.2e-14
Δ mean = 1.1
p-value = 8.6e-10
Δ mean = 0.7
Mean protein Intensity (log2)
M/-/-
M/4SU/-
M/4SU/Fvo
V/4SU/-
V/4SU/Fvo
G
V/4SU/Fvo
V/4SU/-
Adj. p-value[-log10]
E2
nsP1
nsP4
Capsid
nsP2
nsP3
Fold change[log2]
V/4SU/- vs V/4SU/Fvo
H
Number of enriched proteins
V/4SU/Fvo
V/4SU/-
I
RNA binding domains
Classical
Non-classical
Both
Other
percentage of proteins
MitoRNP
cRNP
vRNP
cRNPen
vRNPen
J
Percentage of disordered region
MitoRNP
cRNPen
vRNPen
K
Genomic RNA
Nonstructural polyprotein
Structural polyprotein
AAAAn
Early
Late
Subgenmic RNA
CP
E3
E2
6K
E1
AAAAn
P123
P123
nsP4
nsP1
nsP2
nsP3
nsP4
CP
E3
E2
6K
E1

Figure S2

Figure S2. Proteomic analysis of SINV RNPs.

A-E) Scatter plots showing protein intensity correlation across replicates for the different condition shown in Figure 1B. Pearson coefficient and protein intensity distribution are also shown.

F) Box plot showing the distribution of protein intensities in the experimental and control samples (lower and upper ends of the hinges are defined by the first and third quartile). p-values were estimated by Welch's t-test.

G) Volcano plot showing fold change and adjusted p-value for each protein (dot) comparing V/4SU/- versus V/4SU/Fvo. Proteins enriched within 1% FDR are coloured in red and blue and those within 10% FDR in orange and cyan. Viral proteins are indicated. H) Number of proteins significantly enriched in V/4SU/- and V/4SU/Fvo samples with FDR<10%. Data in G and H shows that V/4SU/Fvo enriched proteins are a subset of V/4SU/-.

I) Proportion of proteins with classical RBDs, nonclassical RBDs, both or none in mitoRNPs, cRNPs, vRNPs, cRNP-enriched (en) and vRNPen.

J) Box plot showing the distribution of intrinsically disorder regions in mitoRNPs, cRNPen and vRNPen.

K) schematic of SINV gRNA, sgRNA and derived viral proteins.

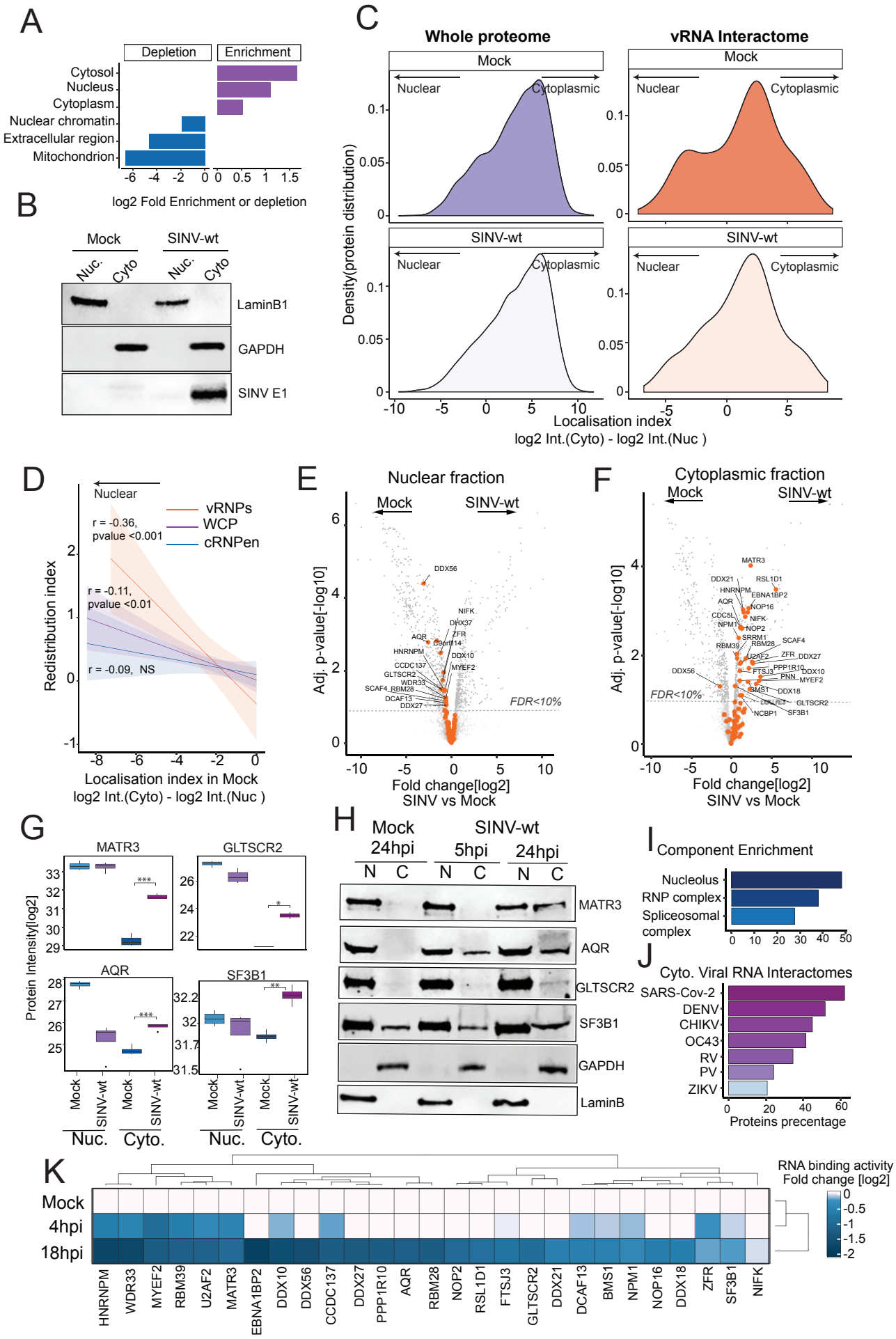
A
Depletion
Enrichment
Cytosol
Nucleus
Cytoplasm
Nuclear chromatin
Extracellular region
Mitochondrion
log2 Fold Enrichment or depletion
B
Mock
SINV-wt
Nuc.
Cyto
LaminB1
GAPDH
SINV E1
C
Whole proteome
vRNA Interactome
Mock
SINV-wt
Nuclear
Cytoplasmic
Density(protein distribution)
Localisation index
log2 Int.(Cyto) - log2 Int.(Nuc)
D
Nuclear
vRNPs
WCP
cRNPen
r = -0.36, pvalue <0.001
r = -0.11, pvalue <0.01
r = -0.09, NS
Redistribution index
Localisation index in Mock
log2 Int.(Cyto) - log2 Int.(Nuc)
E
Nuclear fraction
Mock
SINV-wt
Adj. p-value[-log10]
FDR<10%
Fold change[log2]
SINV vs Mock
F
Cytoplasmic fraction
Mock
SINV-wt
Adj. p-value[-log10]
FDR<10%
Fold change[log2]
SINV vs Mock
G
MATR3
GLTSCR2
AQR
SF3B1
Protein Intensity[log2]
Mock
SINV-wt
Nuc.
Cyto.
H
Mock 24hpi
SINV-wt 5hpi
SINV-wt 24hpi
N
C
MATR3
AQR
GLTSCR2
SF3B1
GAPDH
LaminB
I
Component Enrichment
Nucleolus
RNP complex
Spliceosomal complex
J
Cyto. Viral RNA Interactomes
SARS-Cov-2
DENV
CHIKV
OC43
RV
PV
ZIKV
Proteins precentage
K
Mock
4hpi
18hpi
RNA binding activity Fold change [log2]
HNRNPM
WDR33
MYEF2
RBM39
U2AF2
MATR3
EBNA1BP2
DDX10
DDX56
CCDC137
DDX27
PPP1R10
AQR
RBM28
NOP2
RSL1D1
FTSJ3
GLTSCR2
DDX21
DCAF13
BMS1
NPM1
NOP16
DDX18
ZFR
SF3B1
NIFK

Figure 3

Figure 3. Nucleo-cytoplasmic redistribution of nuclear vRNP components.

A) Bar plot showing 'cellular component' GO terms related to subcellular localisation that are enriched in vRNPs over the human proteome.

B) Quality control Western blot analysis for the nucleo-cytoplasmic fractionation experiments in mock and SINV-infected cells, using antibodies against the cytoplasmic protein marker GAPDH, nuclear membrane protein marker Lamin B and and cytoplasmic SINV E1 glycoprotein.

C) Kernel density analysis of the protein localisation index, which estimated as the [log2] ratio of protein intensity in the cytoplasmic fraction over the nuclear fraction. Density plots are shown for the proteins within the WCP and vRNPs in both mock-infected and SINV-infected cells.

D) Linear regression analysis of the localisation index against the redistribution index (i.e. fold change between the localisation index of each protein in SINV infected and mock cells) for the proteins within vRNPs, cRNPen, and total proteome (WCP) (related to Figure S3D).

E-F) Volcano plots showing the fold change and p-value for each protein in the nuclear (E) and cytoplasmic fractions (F) of SINV- and mock-infected cells.

G) Box plots showing the intensities of MATR3, GLTSCR2, AQR and SF3B1 in the cytoplasmic and nuclear fractions in mock and infected cells (lower and upper ends of the hinges are defined by the first and third quartile). *, ** and *** indicate FDR < 10, 5 and 1%, respectively.

H) Immunoblotting of the representative proteins from (G), in the nuclear and cytoplasmic fraction of SINV-infected (5 and 24hpi) and uninfected cells. GAPDH and laminB1 were used for quality control of the fractionation.

I) Bar plot showing 'cellular component' GO terms enriched in the nuclear components of vRNPs displaying cytoplasmic relocalisation in infected cells.

J) Proportion of the proteins in (I) that have been reported to interact with the RNAs of other cytoplasmic viruses. Data compiled extracted from (Iselin et al., 2021).

K) Heatmap showing the alterations in RNA-binding activity induced by SINV infection for the proteins in (I). Data from (Garcia-Moreno et al., 2019).

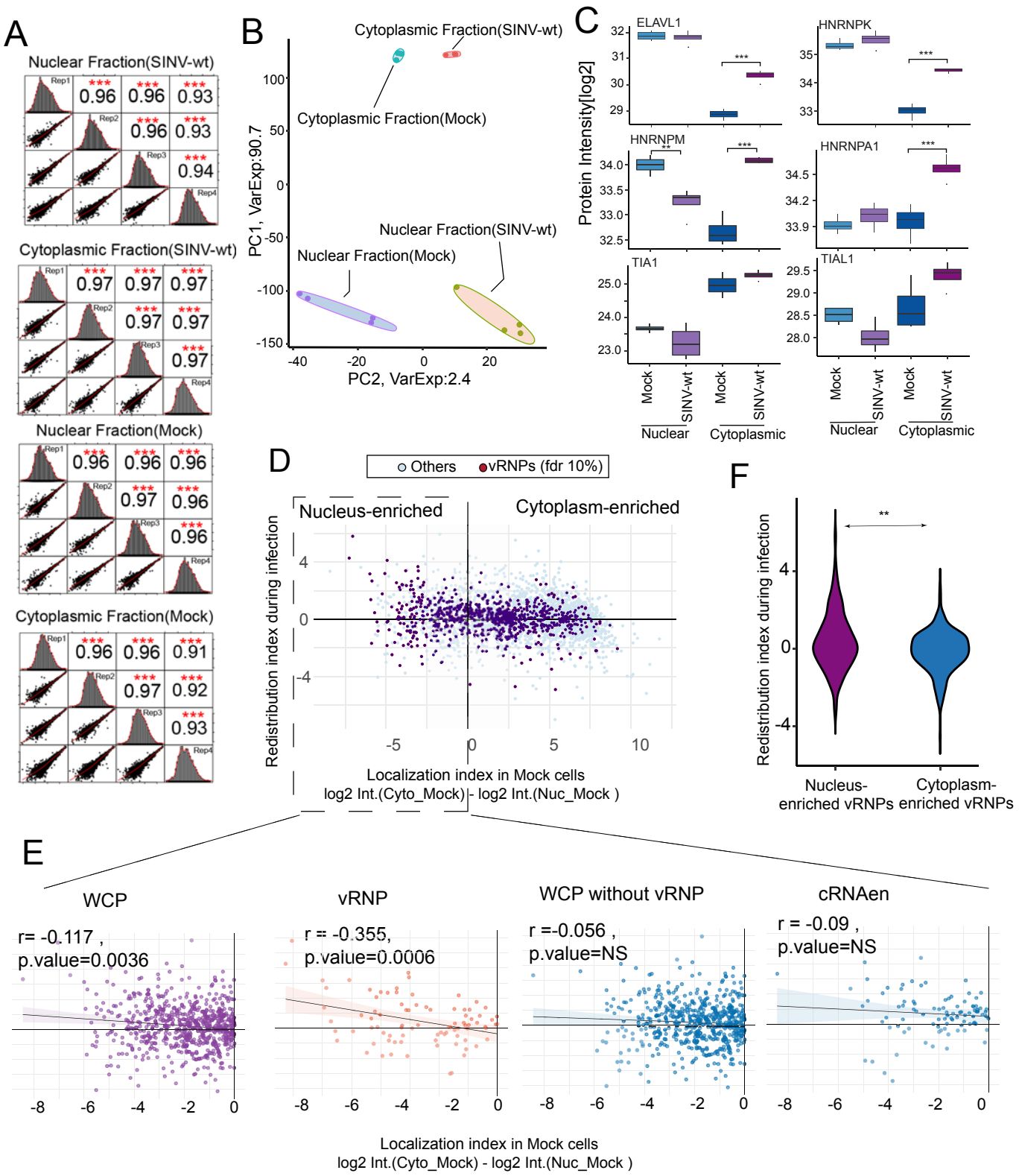
A
Nuclear Fraction(SINV-wt)
Cytoplasmic Fraction(SINV-wt)
Nuclear Fraction(Mock)
Cytoplasmic Fraction(Mock)
B
Cytoplasmic Fraction(SINV-wt)
Cytoplasmic Fraction(Mock)
Nuclear Fraction(SINV-wt)
Nuclear Fraction(Mock)
PC1, VarExp:90.7
PC2, VarExp:2.4
C
ELAVL1
HNRNPK
HNRNPM
HNRNPA1
TIA1
TIAL1
Protein Intensity[log2]
Mock
SINV-wt
Nuclear
Cytoplasmic
D
Others
vRNPs (fdr 10%)
Nucleus-enriched
Cytoplasm-enriched
Redistribution index during infection
Localization index in Mock cells
log2 Int.(Cyto_Mock) - log2 Int.(Nuc_Mock)
F
Redistribution index during infection
Nucleus-enriched vRNPs
Cytoplasm-enriched vRNPs
E
WCP
r= -0.117 ,
p.value=0.0036
vRNP
r = -0.355,
p.value=0.0006
WCP without vRNP
r =-0.056 ,
p.value=NS
cRNAen
r = -0.09 ,
p.value=NS
Localization index in Mock cells
log2 Int.(Cyto_Mock) - log2 Int.(Nuc_Mock)

Figure S3

Figure 3S. Proteomic analysis of nucleus and cytoplasm in SINV infected cells.

A) Scatter plots showing protein intensity correlation in nuclear and cytoplasmic fractions in mock- and SINV-infected cells. Pearson coefficient and protein intensity distribution are also shown.

B) Principal component analysis of the nuclear and cytoplasmic fractions of mock- and SINV-infected cells.

C) Intensities of selected proteins in the nucleus and cytoplasm of mock- and SINV-infected cells. These proteins were previously shown to relocate to the cytoplasm in alphavirus infected cells. *, ** and *** indicate FDR < 10, 5 and 1% respectively.

D) Scatter plot comparing the localisation index in mock to the redistribution index (localisation index in infected - localisation index mock cells).

E) Linear regression analysis of localisation index against redistribution index for following protein subgroups: whole cell proteome (WCP), vRNPs, WCP without vRNP components, and cRNPen.

F) Violin plot showing the distribution of the redistribution index across the proteins within nuclear and cytoplasmic components of vRNPs. ** indicate p-value <0.05 estimated by Welch's t-test.

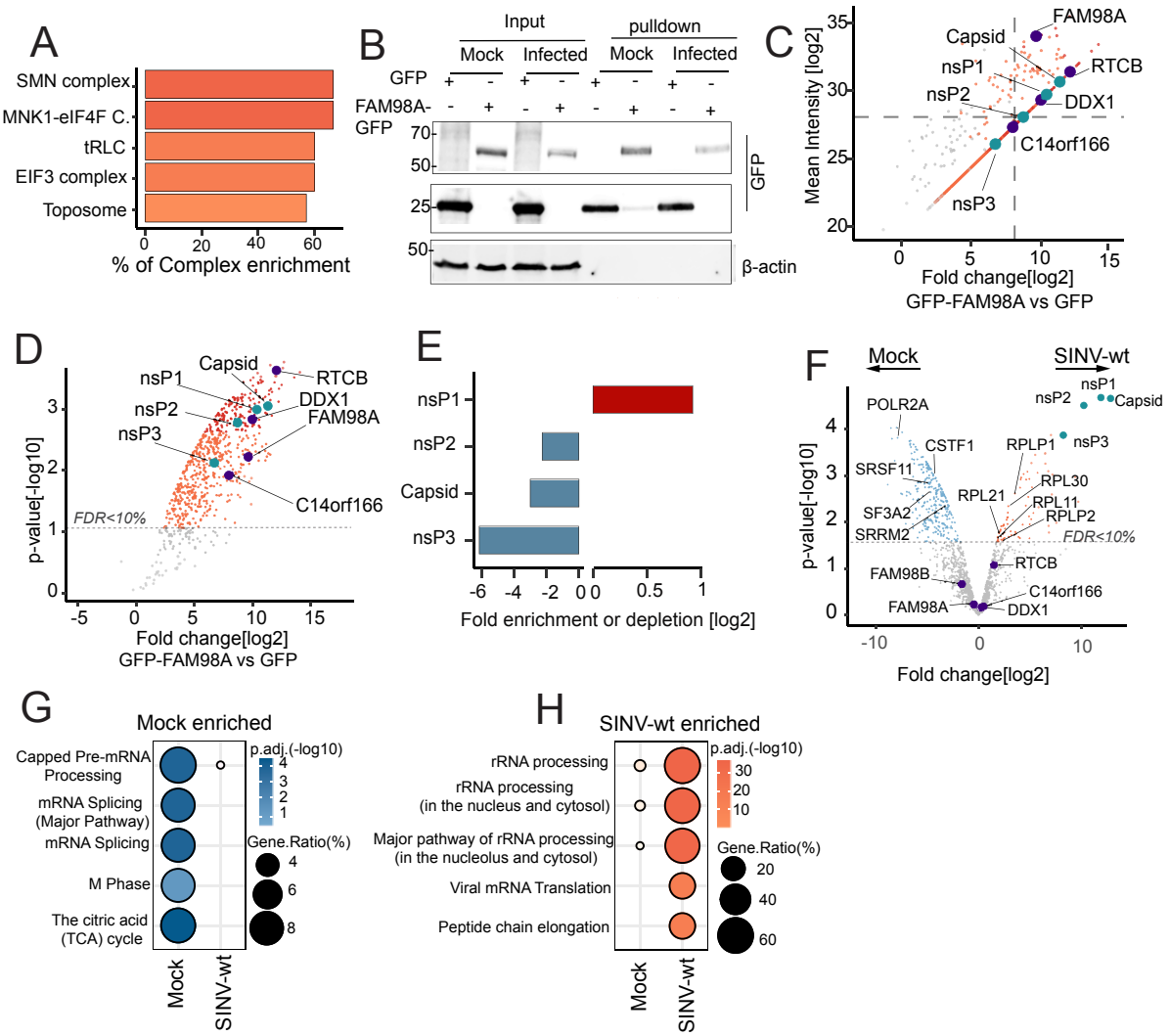
A
SMN complex
MNK1-eIF4F C.
tRLC
EIF3 complex
Toposome
0
20
40
60
% of Complex enrichment
B
Input
pulldown
Mock
Infected
Mock
Infected
GFP
FAM98A-GFP
70
50
25
50
GFP
β-actin
C
Mean Intensity [log2]
FAM98A
Capsid
nsP1
RTCB
nsP2
DDX1
C14orf166
nsP3
Fold change[log2]
GFP-FAM98A vs GFP
D
p-value[-log10]
Capsid
nsP1
RTCB
nsP2
DDX1
nsP3
FAM98A
C14orf166
FDR<10%
Fold change[log2]
GFP-FAM98A vs GFP
E
nsP1
nsP2
Capsid
nsP3
Fold enrichment or depletion [log2]
F
Mock
SINV-wt
p-value[-log10]
POLR2A
nsP2
nsP1
Capsid
CSTF1
RPLP1
nsP3
SRSF11
RPL30
RPL21
RPL11
SF3A2
RPLP2
SRRM2
FDR<10%
RTCB
FAM98B
C14orf166
FAM98A
DDX1
Fold change[log2]
G
Mock enriched
Capped Pre-mRNA Processing
mRNA Splicing (Major Pathway)
mRNA Splicing
M Phase
The citric acid (TCA) cycle
p.adj.(-log10)
Gene.Ratio(%)
Mock
SINV-wt
H
SINV-wt enriched
rRNA processing
rRNA processing (in the nucleus and cytosol)
Major pathway of rRNA processing (in the nucleolus and cytosol)
Viral mRNA Translation
Peptide chain elongation
p.adj.(-log10)
Gene.Ratio(%)
Mock
SINV-wt

Figure 4

Figure 4. Changes in the tRNA-LC interactome in SINV-infected cells.

A) Bar plot showing protein complexes ranked based on the enrichment of their components in SINV vRNPs, taking into consideration if their RNA-binding activity increased throughout infection (Data from Garcia-Moreno et al., 2019).

B) Detection by Western blot of unfused eGFP and FAM98A-eGFP in inputs and eluates of GFP-IPs.

C) MA-plot showing the intensity of each protein in FAM98A-eGFP eluates and the fold change between FAM98A-eGFP and eGFP IPs. Dashed lines delimit the top 75% quantile of the FAM98A interactome.

D) Volcano plot showing fold change of each protein in FAM98A-eGFP versus eGFP IPs and the adjusted p-value. Proteins enriched in FAM98A-GFP within 1% FDR are coloured in red and proteins within 10% FDR in orange.

E) Bar plot showing the fold change [log2] of viral proteins in FAM98A-GFP eluates normalised to that in the WCP.

F) Volcano plot showing the fold changes and p-value of proteins in FAM98A-eGFP IP eluates in SINV-infected and mock cells. Proteins that associated differentially with FAM98A-eGFP in mock and infected cells are coloured in red or blue (FDR<10%). Viral proteins are shown in green and tRNA-LC components in violet.

G-H) Pathway Enrichment Analysis of FAM98A-GFP interactors enriched in (G) Mock cells, and in (H) SINV-infected cells.

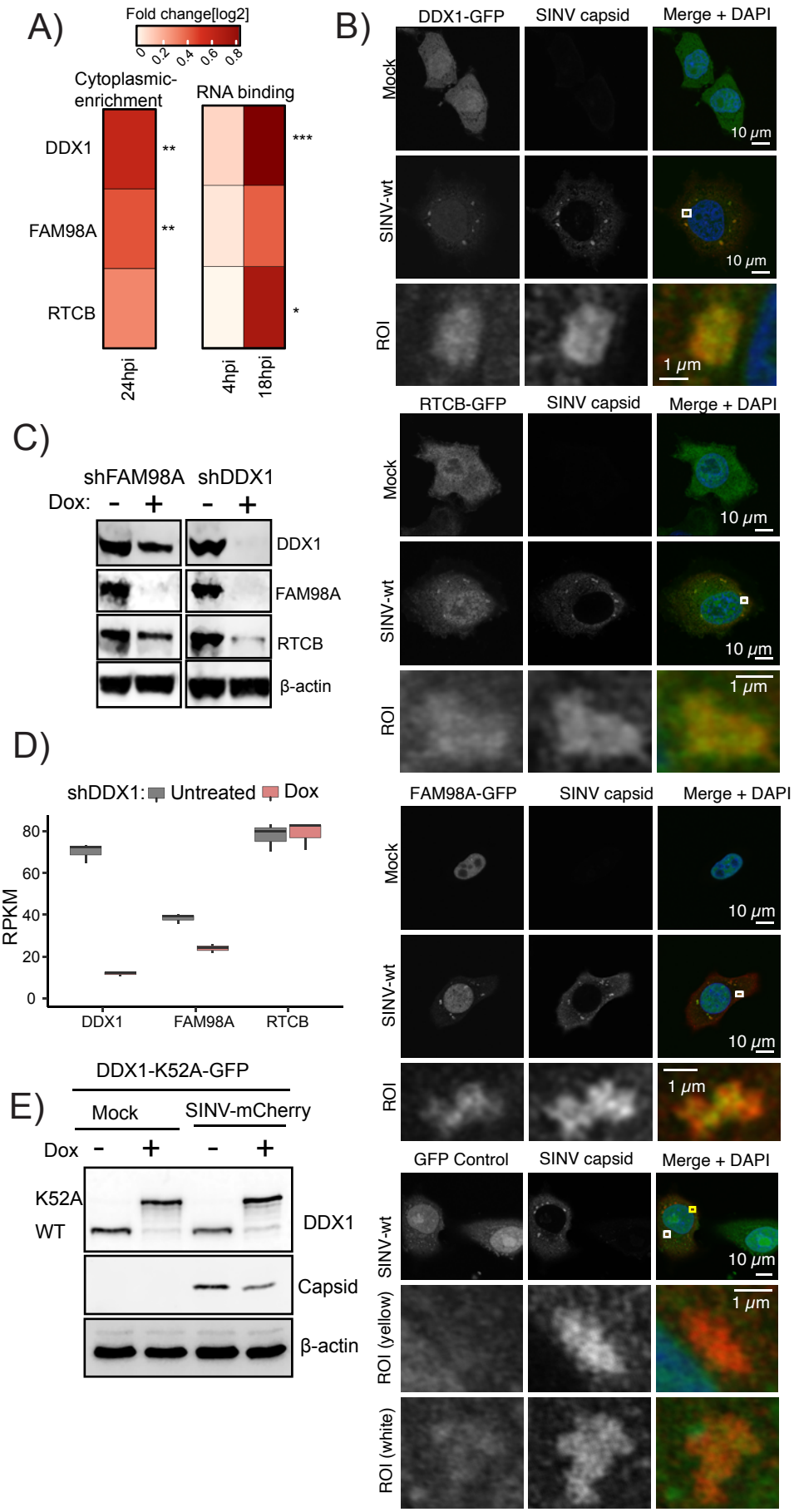
A)
Fold change[log2]
0
0.2
0.4
0.6
0.8
Cytoplasmic-enrichment
RNA binding
DDX1
FAM98A
RTCB
**
**
***
*
24hpi
4hpi
18hpi
B)
DDX1-GFP
SINV capsid
Merge + DAPI
Mock
SINV-wt
ROI
10 μm
1 μm
RTCB-GFP
FAM98A-GFP
GFP Control
ROI (yellow)
ROI (white)
C)
shFAM98A
shDDX1
Dox:
-
+
DDX1
FAM98A
RTCB
β-actin
D)
shDDX1: Untreated Dox
RPKM
80
60
40
20
0
DDX1
FAM98A
RTCB
E)
DDX1-K52A-GFP
Mock
SINV-mCherry
Dox
K52A
WT
DDX1
Capsid
β-actin

Figure S4

Figure S4. The tRNA-LC in SINV infected cells.

A) Heat map showing the fold enrichment [log2] of the tRNA-LC components identified in vRNPs (i.e. DDX1, FAM98A and RTCB) in the cytoplasmic fraction (left panel) and in the RNA-bound fraction (right panel; data from Garcia-Moreno et al., 2019) during SINV [MOI= 10] infection. *, ** and *** indicate FDR < 10, 5 and 1% respectively.

B) Confocal localisation analysis of FAM98A-eGFP, DDX1-eGFP and RTCB-eGFP in mock and SINV infected cells. An antibody against SINV capsid was used to localise the viral factories.

C) Western blot analysis of FAM98A, DDX1 and RTCB in shFAM98A and shDDX1 HEK293 cells, uninduced or induced with doxycycline (Dox) for 48 hours. β-actin was used as loading control.

D) Abundance of *fam98a*, *ddx1* and rtcb mRNAs in shDDX1 HEK293 cells, uninduced or induced with doxycycline for 48 hours and analysed by RNAseq, (RPKM) Reads Per Kilobase of transcript per Million mapped reads.

E) Western blot analysis of SINV capsid levels in HEK293 cells expressing DDX1-K52A and infected or not with SINV for 18h (MOI= 0.1). Levels of DDX1 and ß-actin were also analysed.

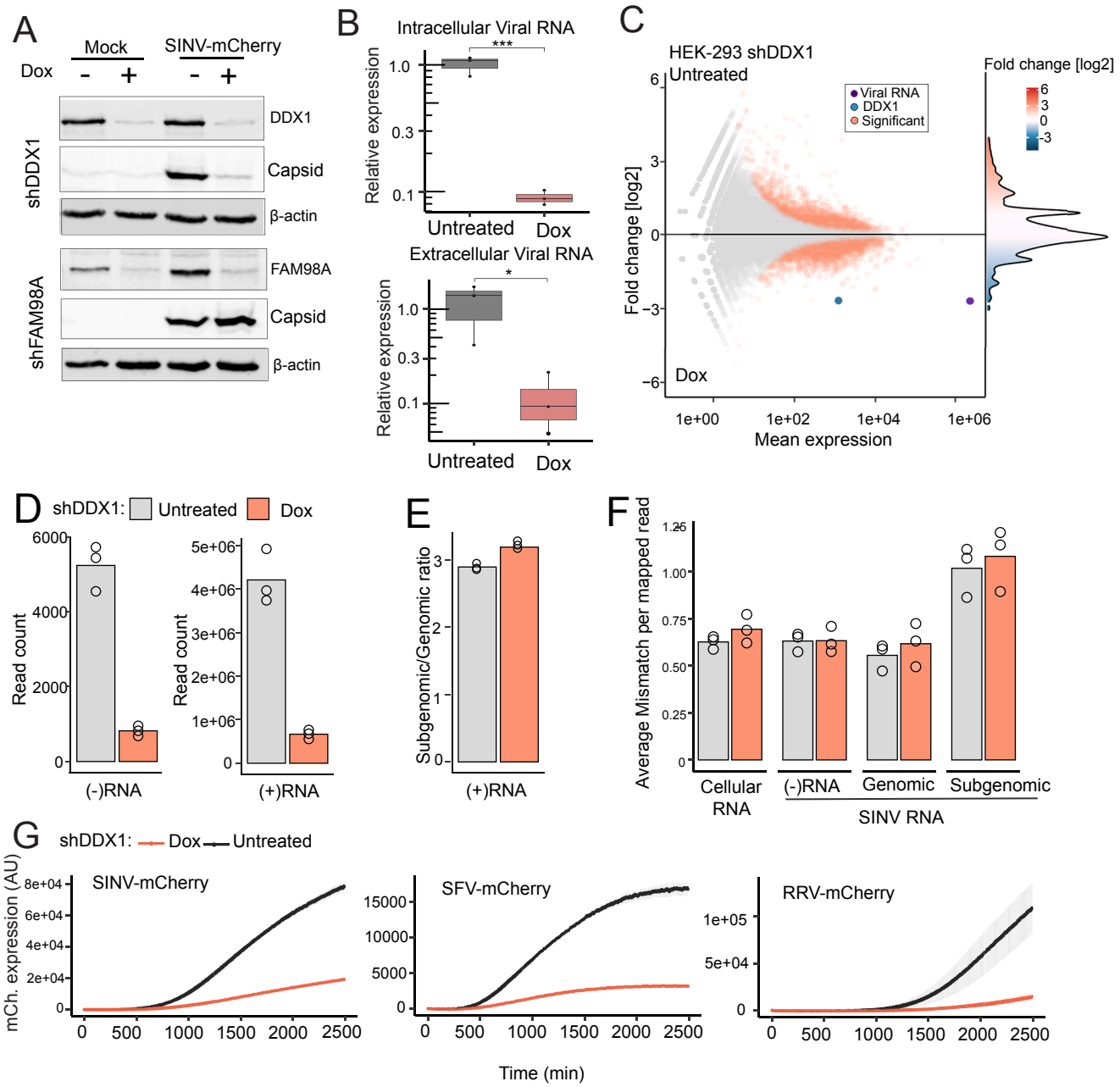
A
Mock
SINV-mCherry
Dox
- + - +
shDDX1
DDX1
Capsid
β-actin
shFAM98A
FAM98A
Capsid
β-actin
B
Intracellular Viral RNA
Relative expression
Untreated
Dox
Extracellular Viral RNA
Relative expression
Untreated
Dox
C
HEK-293 shDDX1
Untreated
Dox
Viral RNA
DDX1
Significant
Fold change [log2]
Fold change [log2]
Mean expression
D
shDDX1: Untreated Dox
Read count
(-)RNA
(+)RNA
E
Subgenomic/Genomic ratio
(+)RNA
F
Average Mismatch per mapped read
Cellular RNA
(-)RNA
Genomic
Subgenomic
SINV RNA
G
shDDX1: Dox Untreated
mCh. expression (AU)
SINV-mCherry
SFV-mCherry
RRV-mCherry
Time (min)

Figure 5

Figure 5. the tRNA-LC regulates SINV replication.

A) Western blot analysis of SINV capsid levels in shFAM98A and shDDX1 HEK293 cells SINV or mock infected for 18h (MOI= 0.1). Levels of DDX1, FAM98A and ß-actin were also analysed.

B) RT-qPCR analysis showing abundance of SINV genomic RNA in Dox-treated shDDX1 HEK293 cells relative to untreated cells, both in cell pellets (intracellular genomic (g)RNA) and supernatant (extracellular gRNA). *, ** and *** indicate student t-test p-value < 0.1, 0.05 and 0.001 respectively.

C-F) Dox-treated and untreated shDDX1 cells were infected with SINV for 18h (MOI= 0.1) or mock-infected and analysed by RNAseq.

C) MA plot showing the mean expression of each

RNA and their fold change in Dox-treated versus untreated shDDX1 HEK293 cells.

D) Read counts mapping to positive or negative strand of SINV RNA [i.e. (+)RNA and (-)RNA].

E) Ratio between the reads mapping to the gRNA/sgRNA overlap (last 1/3 of the genome) and those mapping to the gRNA (first 2/3 of the genome).

F) Average mismatch per mapped read in cellular RNA and different subtypes of viral RNA.

G) Graph showing red fluorescent signal derived from SINV-mCherry, SFV-mChery and RRV-mCherry in shDDX1 HEK293 cells Dox-treated or untreated. Fluorescence was measured every 15 min over a period of 36 h. Error bars indicate standard deviation, n=3.

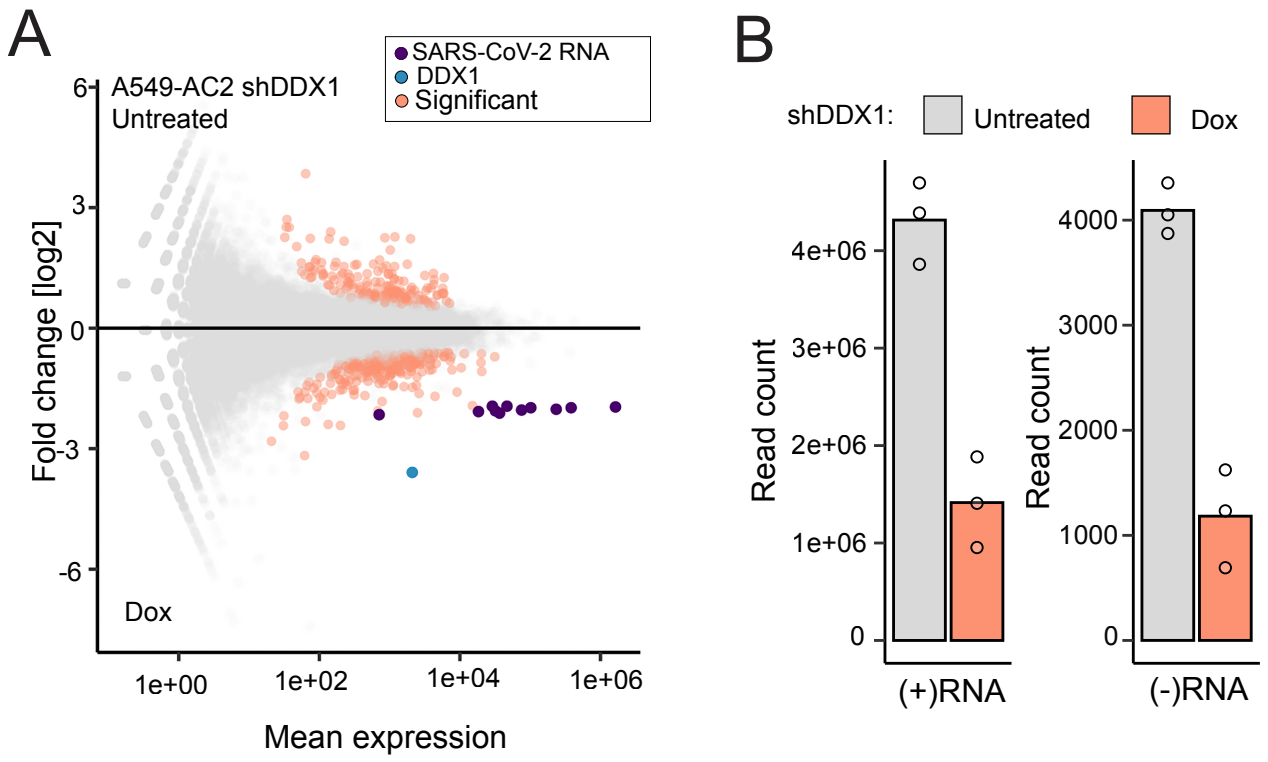
A
A549-AC2 shDDX1
Untreated
Dox
SARS-CoV-2 RNA
DDX1
Significant
Fold change [log2]
6
3
0
-3
-6
1e+00
1e+02
1e+04
1e+06
Mean expression
B
shDDX1:
Untreated
Dox
Read count
4e+06
3e+06
2e+06
1e+06
0
(+)RNA
Read count
4000
3000
2000
1000
0
(-)RNA

Figure 5S

Figure S5. tRNA-LC also controls SARS-CoV-2 replication.

A-B) Dox-treated and untreated shDDX1 A549-ACE2 cells were infected with SARS-CoV-2 for 24h (MOI= 0.1).

A) MA plot of mean genes expression and fold change between DDX1 KD and untreated cells.

B) read count mapping to the positive and negative RNA strands of SARS-CoV-2 genome upon depletion of DDX1.

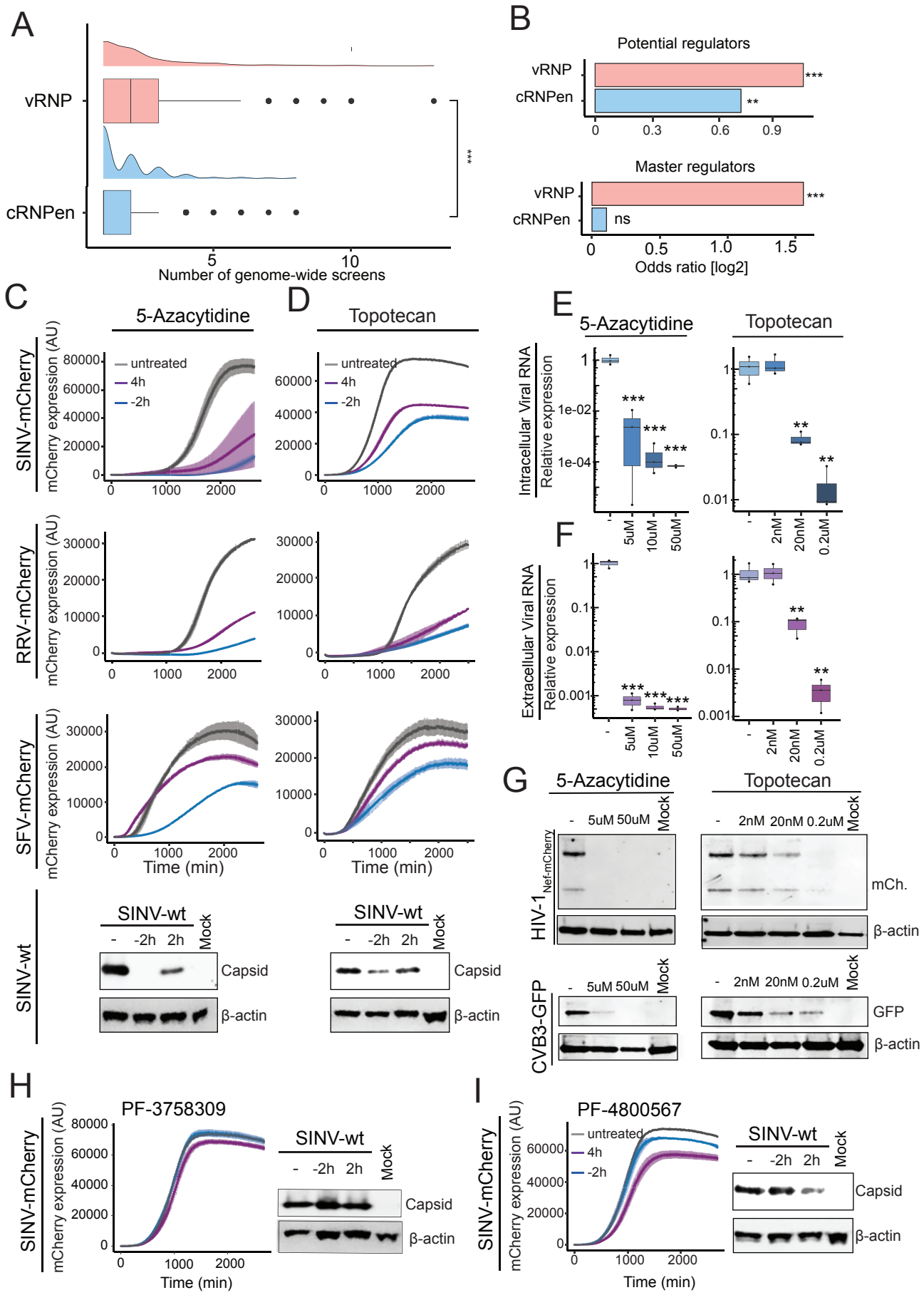
A
vRNP
cRNPen
***
5
10
Number of genome-wide screens
B
Potential regulators
vRNP
cRNPen
***
**
0
0.3
0.6
0.9
Master regulators
vRNP
cRNPen
***
ns
0
0.5
1.0
1.5
Odds ratio [log2]
C
5-Azacytidine
D
Topotecan
SINV-mCherry
RRV-mCherry
SFV-mCherry
mCherry expression (AU)
untreated
4h
-2h
Time (min)
SINV-wt
-
-2h
2h
Mock
Capsid
β-actin
E
5-Azacytidine
Topotecan
Intracellular Viral RNA
Relative expression
5uM
10uM
50uM
2nM
20nM
0.2uM
F
Extracellular Viral RNA
Relative expression
G
5-Azacytidine
Topotecan
HIV-1
Nef-mCherry
mCh.
CVB3-GFP
GFP
β-actin
H
PF-3758309
SINV-mCherry
SINV-wt
Capsid
β-actin
I
PF-4800567
SINV-mCherry
SINV-wt
Capsid
β-actin

Figure 6

Figure 6. Components of SINV RNPs as targets for broad-spectrum therapies.

A) Distribution of genome wide screen hits within vRNP or cRNPen datasets. B) Bar plot showing the enrichment of potential regulators (protein reported in three screens) and master regulators (proteins linked to three different virus families in at least three screens) in vRNP or cRNPen datasets.

C- D) Effect 5-Azacytidine and Topotecan on alphavirus replication. Upper panels, SINV-mCherry, RRV-mCherry and SFV-mCherry fitness in presence of different doses of either inhibitor. mCherry expression was measured as in Figure 5G. Error bars indicate standard deviation, n=3, 4h and -2h indicate times of drug-treatment relative to start of infection. Lower panel, analysis of SINV capsid expression by Western blot in cells treated with either inhibitor analysed, 2h and -2h indicate times of drug-treatment relative to start of infection.

E-F) qRT-PCR analysis of SINV intracellular (in cell pellet) (E) and extracellular (in supernatant) (F) gRNA in cells treated with different doses of 5-Azacytidine or Topotecan. *, ** and *** indicate student t-test p-value < 0.1, 0.05 and 0.001 respectively, n=3. G) Immunoblotting of mCherry or GFP in HIV-$1_{Nef\text{-}mCherry}$ or CVB3-GFP infected cells, respectively.

H-I) effect of PF-480056 and PF-375830 on SINV-mCherry measuring red fluorescence as in Figure 5G, or on SINV-wt by Western blot analysis of capsid expression.

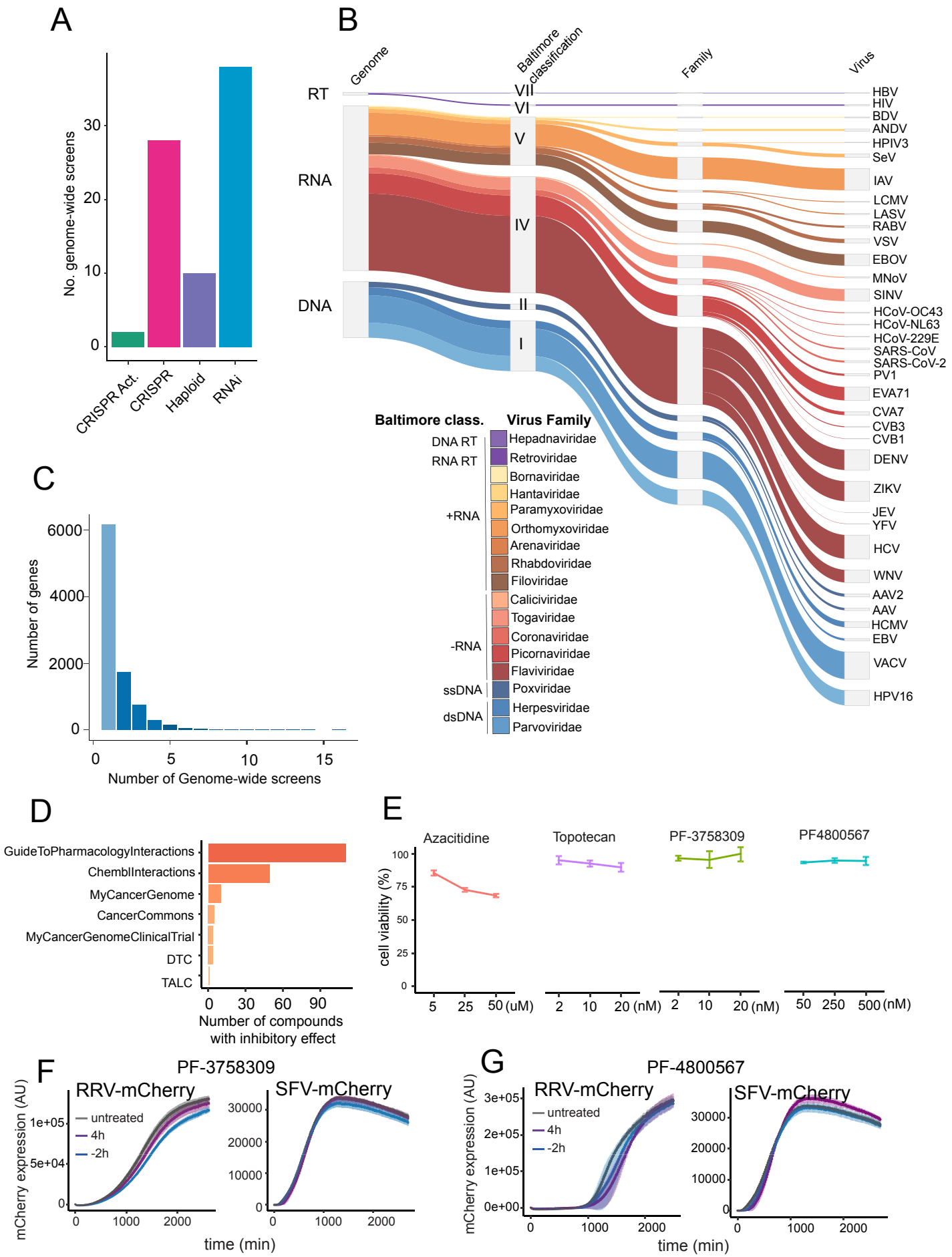
A
No. genome-wide screens
CRISPR Act.
CRISPR
Haploid
RNAi
B
Genome
Baltimore classification
Family
Virus
RT
RNA
DNA
VII
VI
V
IV
II
I
HBV
HIV
BDV
ANDV
HPIV3
SeV
IAV
LCMV
LASV
RABV
VSV
EBOV
MNoV
SINV
HCoV-OC43
HCoV-NL63
HCoV-229E
SARS-CoV
SARS-CoV-2
PV1
EVA71
CVA7
CVB3
CVB1
DENV
ZIKV
JEV
YFV
HCV
WNV
AAV2
AAV
HCMV
EBV
VACV
HPV16
Baltimore class.
Virus Family
DNA RT
RNA RT
+RNA
-RNA
ssDNA
dsDNA
Hepadnaviridae
Retroviridae
Bornaviridae
Hantaviridae
Paramyxoviridae
Orthomyxoviridae
Arenaviridae
Rhabdoviridae
Filoviridae
Caliciviridae
Togaviridae
Coronaviridae
Picornaviridae
Flaviviridae
Poxviridae
Herpesviridae
Parvoviridae
C
Number of genes
Number of Genome-wide screens
D
GuideToPharmacologyInteractions
ChemblInteractions
MyCancerGenome
CancerCommons
MyCancerGenomeClinicalTrial
DTC
TALC
Number of compounds with inhibitory effect
E
Azacitidine
Topotecan
PF-3758309
PF4800567
cell viability (%)
(uM)
(nM)
F
PF-3758309
RRV-mCherry
SFV-mCherry
untreated
4h
-2h
mCherry expression (AU)
time (min)
G
PF-4800567
RRV-mCherry
SFV-mCherry
untreated
4h
-2h
mCherry expression (AU)
time (min)

Figure S6

Figure S6. Relevance of vRNP components in virus infection. A) Bar plot summarising the number of studies for each genome-wide screening strategy.

B) Outline of the Baltimore classification of the different viruses covered in the genome wide screens. Line thickness relates to the total number of reported “hits” (genes).

C) Bar plot showing the relationship between genes and number of screens reporting them as ‘hits’.

D) Number of compounds targeting SINV vRNP components listed in different drug databases.

E) Effects of the different drugs and their doses on cell viability relative to the untreated control.

F-G) Effect of PF-480056 and PF-375830 on SFV-Cherry and RRV-mCherry. Red fluorescence was measured as in Figure 5G and error bars represent standard deviation, n=3, 4h and -2h indicate time of drug-treatment relative to start of infection.

REFERENCES

Aouadi, M., Tesz, G.J., Nicoloro, S.M., Wang, M., Chouinard, M., Soto, E., Ostroff, G.R., and Czech, M.P. (2009). Orally delivered siRNA targeting macrophage Map4k4 suppresses systemic inflammation. Nature *458*, 1180-1184.

Aviner, R., Li, K.H., Frydman, J., and Andino, R. (2021). Cotranslational prolyl hydroxylation is essential for flavivirus biogenesis. Nature *596*, 558-564.

Balistreri, G., Horvath, P., Schweingruber, C., Zund, D., McInerney, G., Merits, A., Muhlemann, O., Azzalin, C., and Helenius, A. (2014). The host nonsense-mediated mRNA decay pathway restricts Mammalian RNA virus replication. Cell Host Microbe *16*, 403-411.

Barchiesi, A., and Vascotto, C. (2019). Transcription, Processing, and Decay of Mitochondrial RNA in Health and Disease. Int J Mol Sci *20*.

Beckmann, B.M., Horos, R., Fischer, B., Castello, A., Eichelbaum, K., Alleaume, A.M., Schwarzl, T., Curk, T., Foehr, S., Huber, W.*, et al.* (2015). The RNA-binding proteomes from yeast to man harbour conserved enigmRBPs. Nat Commun *6*, 10127.

Bonizzoni, M., Gasperi, G., Chen, X., and James, A.A. (2013). The invasive mosquito species Aedes albopictus: current knowledge and future perspectives. Trends Parasitol *29*, 460-468.

Carrasco, L., Sanz, M.A., and Gonzalez-Almela, E. (2018). The Regulation of Translation in Alphavirus-Infected Cells. Viruses *10*.

Castello, A., Fischer, B., Eichelbaum, K., Horos, R., Beckmann, B.M., Strein, C., Davey, N.E., Humphreys, D.T., Preiss, T., Steinmetz, L.M.*, et al.* (2012). Insights into RNA Biology from an Atlas of Mammalian mRNA-Binding Proteins. Cell *149*, 1393-1406.

Castello, A., Fischer, B., Frese, C.K., Horos, R., Alleaume, A.M., Foehr, S., Curk, T., Krijgsveld, J., and Hentze, M.W. (2016). Comprehensive Identification of RNA-Binding Domains in Human Cells. Mol Cell *63*, 696-710.

Castello, A., Horos, R., Strein, C., Fischer, B., Eichelbaum, K., Steinmetz, L.M., Krijgsveld, J., and Hentze, M.W. (2013). System-wide identification of RNA-binding proteins by interactome capture. Nat Protoc *8*, 491-500.

Castello, A., Sanz, M.A., Molina, S., and Carrasco, L. (2006). Translation of Sindbis virus 26S mRNA does not require intact eukariotic initiation factor 4G. J Mol Biol *355*, 942-956.

Choudhury, N.R., Heikel, G., Trubitsyna, M., Kubik, P., Nowak, J.S., Webb, S., Granneman, S., Spanos, C., Rappsilber, J., Castello, A.*, et al.* (2017). RNA-binding activity of TRIM25 is mediated by its PRY/SPRY domain and is required for ubiquitination. BMC Biol *15*, 105.

Cotto, K.C., Wagner, A.H., Feng, Y.Y., Kiwala, S., Coffman, A.C., Spies, G., Wollam, A., Spies, N.C., Griffith, O.L., and Griffith, M. (2018). DGIdb 3.0: a redesign and expansion of the drug-gene interaction database. Nucleic Acids Res *46*, D1068-D1073.

Cox, J., Neuhauser, N., Michalski, A., Scheltema, R.A., Olsen, J.V., and Mann, M. (2011). Andromeda: a peptide search engine integrated into the MaxQuant environment. J Proteome Res *10*, 1794-1805.

Dhir, A., Dhir, S., Borowski, L.S., Jimenez, L., Teitell, M., Rotig, A., Crow, Y.J., Rice, G.I., Duffy, D., Tamby, C.*, et al.* (2018). Mitochondrial double-stranded RNA triggers antiviral signalling in humans. Nature *560*, 238-242.

Dicker, K., Jarvelin, A.I., Garcia-Moreno, M., and Castello, A. (2020). The importance of virion-incorporated cellular RNA-Binding Proteins in viral particle assembly and infectivity. Semin Cell Dev Biol.

Flynn, R.A., Belk, J.A., Qi, Y., Yasumoto, Y., Wei, J., Alfajaro, M.M., Shi, Q., Mumbach, M.R., Limaye, A., DeWeirdt, P.C.*, et al.* (2021). Discovery and functional interrogation of SARS-CoV-2 RNA-host protein interactions. Cell *184*, 2394-2411 e2316.

Frolova, E.I., Gorchakov, R., Pereboeva, L., Atasheva, S., and Frolov, I. (2010). Functional Sindbis virus replicative complexes are formed at the plasma membrane. J Virol *84*, 11679-11695.

Fukuchi, S., Hosoda, K., Homma, K., Gojobori, T., and Nishikawa, K. (2011). Binary classification of protein molecules into intrinsically disordered and ordered segments. BMC Struct Biol *11*, 29.

Fukuhara, T., Hosoya, T., Shimizu, S., Sumi, K., Oshiro, T., Yoshinaka, Y., Suzuki, M., Yamamoto, N., Herzenberg, L.A., Herzenberg, L.A.*, et al.* (2006). Utilization of host SR protein kinases and RNA-splicing machinery during viral replication. Proc Natl Acad Sci U S A *103*, 11329-11333.

Gao, Y., Goonawardane, N., Ward, J., Tuplin, A., and Harris, M. (2019). Multiple roles of the non-structural protein 3 (nsP3) alphavirus unique domain (AUD) during Chikungunya virus genome replication and transcription. PLoS Pathog *15*, e1007239.

Garcia-Moreno, M., Jarvelin, A.I., and Castello, A. (2018). Unconventional RNA-binding proteins step into the virus-host battlefront. Wiley Interdiscip Rev RNA *9*, e1498.

Garcia-Moreno, M., Noerenberg, M., Ni, S., Jarvelin, A.I., Gonzalez-Almela, E., Lenz, C.E., Bach-Pages, M., Cox, V., Avolio, R., Davis, T.*, et al.* (2019). System-wide Profiling of RNA-Binding Proteins Uncovers Key Regulators of Virus Infection. Mol Cell.

Gebhart, N.N., Hardy, R.W., and Sokoloski, K.J. (2020). Comparative analyses of alphaviral RNA:Protein complexes reveals conserved host-pathogen interactions. PLoS One *15*, e0238254.

Giurgiu, M., Reinhard, J., Brauner, B., Dunger-Kaltenbach, I., Fobo, G., Frishman, G., Montrone, C., and Ruepp, A. (2019). CORUM: the comprehensive resource of mammalian protein complexes-2019. Nucleic Acids Res *47*, D559-D563.

Gotte, B., Liu, L., and McInerney, G.M. (2018). The Enigmatic Alphavirus Non-Structural Protein 3 (nsP3) Revealing Its Secrets at Last. Viruses *10*.

Haubrich, K., Augsten, S., Simon, B., Masiewicz, P., Perez, K., Lethier, M., Rittinger, K., Gabel, F., Cusack, S., and Hennig, J. (2020). RNA binding regulates TRIM25-mediated RIG-I ubiquitylation. BioRxiv.

Hentze, M.W., Castello, A., Schwarzl, T., and Preiss, T. (2018). A brave new world of RNA-binding proteins. Nat Rev Mol Cell Biol.

Hernandez-Diaz, T., Valiente-Echeverria, F., and Soto-Rifo, R. (2021). RNA Helicase DDX3: A Double-Edged Sword for Viral Replication and Immune Signaling. Microorganisms *9*.

Horos, R., Buscher, M., Kleinendorst, R., Alleaume, A.M., Tarafder, A.K., Schwarzl, T., Dziuba, D., Tischer, C., Zielonka, E.M., Adak, A.*, et al.* (2019). The Small Non-coding Vault RNA1-1 Acts as a Riboregulator of Autophagy. Cell *176*, 1054-1067 e1012.

Hughes, C.S., Moggridge, S., Muller, T., Sorensen, P.H., Morin, G.B., and Krijgsveld, J. (2019). Single-pot, solid-phase-enhanced sample preparation for proteomics experiments. Nat Protoc *14*, 68-85.

Hull, C.M., and Bevilacqua, P.C. (2016). Discriminating Self and Non-Self by RNA: Roles for RNA Structure, Misfolding, and Modification in Regulating the Innate Immune Sensor PKR. Acc Chem Res *49*, 1242-1249.

Iselin, L., Palmalux, N., Kamel, W., Simmonds, P., Mohammed, S., and Castello, A. (2021). Uncovering viral RNA-host cell interactions on a proteome-wide scale. Trends Biochem Sci.

Jarvelin, A.I., Noerenberg, M., Davis, I., and Castello, A. (2016). The new (dis)order in RNA regulation. Cell Commun Signal *14*, 9.

Jones, R., Bragagnolo, G., Arranz, R., and Reguera, J. (2021). Capping pores of alphavirus nsP1 gate membranous viral replication factories. Nature *589*, 615-619.

Jurkin, J., Henkel, T., Nielsen, A.F., Minnich, M., Popow, J., Kaufmann, T., Heindl, K., Hoffmann, T., Busslinger, M., and Martinez, J. (2014). The mammalian tRNA ligase complex mediates splicing of XBP1 mRNA and controls antibody secretion in plasma cells. EMBO J *33*, 2922-2936.

Kamel, W., Noerenberg, M., Cerikan, B., Chen, H., Jarvelin, A.I., Kammoun, M., Lee, J.Y., Shuai, N., Garcia-Moreno, M., Andrejeva, A.*, et al.* (2021). Global analysis of protein-RNA interactions in SARS-CoV-2-infected cells reveals key regulators of infection. Mol Cell *81*, 2851-2867 e2857.

Kim, B., Arcos, S., Rothamel, K., Jian, J., Rose, K.L., McDonald, W.H., Bian, Y., Reasoner, S., Barrows, N.J., Bradrick, S.*, et al.* (2020). Discovery of Widespread Host Protein Interactions with the Pre-replicated Genome of CHIKV Using VIR-CLASP. Mol Cell *78*, 624-640 e627.

Kurkela, S., Manni, T., Vaheri, A., and Vapalahti, O. (2004). Causative agent of Pogosta disease isolated from blood and skin lesions. Emerg Infect Dis *10*, 889-894.

Laine, M., Luukkainen, R., and Toivanen, A. (2004). Sindbis viruses and other alphaviruses as cause of human arthritic disease. J Intern Med *256*, 457-471.

Lanke, K.H., van der Schaar, H.M., Belov, G.A., Feng, Q., Duijsings, D., Jackson, C.L., Ehrenfeld, E., and van Kuppeveld, F.J. (2009). GBF1, a guanine nucleotide exchange factor for Arf, is crucial for coxsackievirus B3 RNA replication. J Virol *83*, 11940-11949.

LaPointe, A.T., Gebhart, N.N., Meller, M.E., Hardy, R.W., and Sokoloski, K.J. (2018). The Identification and Characterization of Sindbis Virus RNA:Host Protein Interactions. J Virol.

Lazar, C., Gatto, L., Ferro, M., Bruley, C., and Burger, T. (2016). Accounting for the Multiple Natures of Missing Values in Label-Free Quantitative Proteomics Data Sets to Compare Imputation Strategies. J Proteome Res *15*, 1116-1125.

Lee, S., Lee, Y.S., Choi, Y., Son, A., Park, Y., Lee, K.M., Kim, J., Kim, J.S., and Kim, V.N. (2021). The SARS-CoV-2 RNA interactome. Mol Cell *81*, 2838-2850 e2836.

Lim, E.X.Y., Lee, W.S., Madzokere, E.T., and Herrero, L.J. (2018). Mosquitoes as Suitable Vectors for Alphaviruses. Viruses *10*.

Lloyd, R.E. (2015). Nuclear proteins hijacked by mammalian cytoplasmic plus strand RNA viruses. Virology *479-480*, 457-474.

Marks, M., and Marks, J.L. (2016). Viral arthritis. Clin Med (Lond) *16*, 129-134.

Pazo, A., Perez-Gonzalez, A., Oliveros, J.C., Huarte, M., Chavez, J.P., and Nieto, A. (2019). hCLE/RTRAF-HSPC117-DDX1-FAM98B: A New Cap-Binding Complex That Activates mRNA Translation. Front Physiol *10*, 92.

Piovesan, D., Necci, M., Escobedo, N., Monzon, A.M., Hatos, A., Micetic, I., Quaglia, F., Paladin, L., Ramasamy, P., Dosztanyi, Z.*, et al.* (2021). MobiDB: intrinsically disordered proteins in 2021. Nucleic Acids Res *49*, D361-D367.

Popow, J., Englert, M., Weitzer, S., Schleiffer, A., Mierzwa, B., Mechtler, K., Trowitzsch, S., Will, C.L., Luhrmann, R., Soll, D.*, et al.* (2011). HSPC117 is the essential subunit of a human tRNA splicing ligase complex. Science *331*, 760-764.

Popow, J., Jurkin, J., Schleiffer, A., and Martinez, J. (2014). Analysis of orthologous groups reveals archease and DDX1 as tRNA splicing factors. Nature *511*, 104-107.

Sanz, M.A., Garcia-Moreno, M., and Carrasco, L. (2015). Inhibition of host protein synthesis by Sindbis virus: correlation with viral RNA replication and release of nuclear proteins to the cytoplasm. Cell Microbiol *17*, 520-541.

Schmidt, N., Lareau, C.A., Keshishian, H., Ganskih, S., Schneider, C., Hennig, T., Melanson, R., Werner, S., Wei, Y., Zimmer, M.*, et al.* (2020). The SARS-CoV-2 RNA-protein interactome in infected human cells. Nat Microbiol.

Silva, L.A., and Dermody, T.S. (2017). Chikungunya virus: epidemiology, replication, disease mechanisms, and prospective intervention strategies. J Clin Invest *127*, 737-749.

Sokoloski, K.J., Nease, L.M., May, N.A., Gebhart, N.N., Jones, C.E., Morrison, T.E., and Hardy, R.W. (2017). Identification of Interactions between Sindbis Virus Capsid Protein and Cytoplasmic vRNA as Novel Virulence Determinants. PLoS Pathog *13*, e1006473.

Strauss, J.H., and Strauss, E.G. (1994). The alphaviruses: gene expression, replication, and evolution. Microbiol Rev *58*, 491-562.

Temperley, R.J., Wydro, M., Lightowlers, R.N., and Chrzanowska-Lightowlers, Z.M. (2010). Human mitochondrial mRNAs--like members of all families, similar but different. Biochim Biophys Acta *1797*, 1081-1085.

Van Nostrand, E.L., Pratt, G.A., Shishkin, A.A., Gelboin-Burkhart, C., Fang, M.Y., Sundararaman, B., Blue, S.M., Nguyen, T.B., Surka, C., Elkins, K.*, et al.* (2016). Robust transcriptome-wide discovery of RNA-binding protein binding sites with enhanced CLIP (eCLIP). Nat Methods *13*, 508-514.

Ventoso, I., Sanz, M.A., Molina, S., Berlanga, J.J., Carrasco, L., and Esteban, M. (2006). Translational resistance of late alphavirus mRNA to eIF2alpha phosphorylation: a strategy to overcome the antiviral effect of protein kinase PKR. Genes Dev *20*, 87-100.

Wang, P., Meng, W., Han, S.C., Li, C.C., Wang, X.J., and Wang, X.J. (2016). The nucleolar protein GLTSCR2 is required for efficient viral replication. Sci Rep *6*, 36226.

Xu, L., Khadijah, S., Fang, S., Wang, L., Tay, F.P., and Liu, D.X. (2010). The cellular RNA helicase DDX1 interacts with coronavirus nonstructural protein 14 and enhances viral replication. J Virol *84*, 8571-8583.

Yao, H., Song, Y., Chen, Y., Wu, N., Xu, J., Sun, C., Zhang, J., Weng, T., Zhang, Z., Wu, Z.*, et al.* (2020). Molecular Architecture of the SARS-CoV-2 Virus. Cell *183*, 730-738 e713.

Zhang, R., Hryc, C.F., Cong, Y., Liu, X., Jakana, J., Gorchakov, R., Baker, M.L., Weaver, S.C., and Chiu, W. (2011a). 4.4 A cryo-EM structure of an enveloped alphavirus Venezuelan equine encephalitis virus. EMBO J *30*, 3854-3863.

Zhang, Z., Kim, T., Bao, M., Facchinetti, V., Jung, S.Y., Ghaffari, A.A., Qin, J., Cheng, G., and Liu, Y.J. (2011b). DDX1, DDX21, and DHX36 helicases form a complex with the adaptor molecule TRIF to sense dsRNA in dendritic cells. Immunity *34*, 866-878.